Signature of a quantum dimensional transition in the spin-$\frac{1}{2}$ antiferromagnetic Heisenberg model on a square lattice and space reduction in the matrix product state

Lihua Wang* and Kwang S. Kim†

Department of Chemistry, School of Natural Science, Center for Superfunctional Materials, Ulsan National Institute of Science and Technology (UNIST), Ulsan 44919, Republic of Korea

(Received 10 March 2018; revised manuscript received 9 April 2019; published 29 April 2019)

We study the spin-$\frac{1}{2}$ antiferromagnetic Heisenberg model on an $\infty \times N$ square lattice for even N's up to 14. Previously, the nonlinear sigma model perturbatively predicted that its spin-rotational symmetry breaks asymptotically with $N \to \infty$, i.e., when it becomes two dimensional (2D). However, we identify a critical width $N_c = 10$ for which this symmetry breaks spontaneously. It shows the signature of a dimensional transition from one dimensional (1D) including quasi-1D to 2D. The finite-size effect differs from that of the $N \times N$ lattice. The ground-state (GS) energy per site approaches the thermodynamic limit value, in agreement with the previously accepted value, by one order of $1/N$ faster than when using $N \times N$ lattices in the literature. Methodwise, we build and variationally solve a matrix product state (MPS) on a chain, converting the N sites in each rung into an effective site. We show that the area law of entanglement entropy does not apply when N increases in our method and the reduced density matrix of each effective site has a saturating number of dominant diagonal elements with increasing N. These two characteristics make the MPS rank needed to obtain a desired energy accuracy quickly saturate when N is large, making our algorithm efficient for large N's. Furthermore, the latter enables space reduction in MPS. Within the framework of MPS, we prove a theorem that the spin-spin correlation at infinite separation is the square of staggered magnetization and demonstrate that the eigenvalue structure of a building MPS unit of $\langle g|g\rangle$, $|g\rangle$ being the GS is responsible for order, disorder, and quasi-long-range order.

DOI: 10.1103/PhysRevB.99.134441

I. INTRODUCTION

With the advancements of experimental probes on the quantum spin system in both one dimension (1D) [1] and two dimensions (2D) [2], rich ground-state (GS) phases such as the disordered Tomonaga-Luttinger spin liquid and the ordered noncollinear antiferromagnetic state are revealed. An ideal model describing them is the antiferromagnetic spin-$\frac{1}{2}$ Heisenberg model. Such a model on an infinite 1D lattice is not ordered with power-law-decaying spin-spin correlations [3]. But, "more is different" [4]. When a collection of infinite 1D lattices are isotropically coupled to form an $\infty \times N$ square lattice called spin ladder, the GS differs. It is predicted to be not ordered with exponentially decaying correlations in a few quasi-1D lattices [5] but ordered in 2D [6]. (Hereafter, we assume an infinity-by-infinity square lattice in our reference to a 2D lattice and confine the discussion within even N's.) It implies that there is at least one-dimensional transition from 1D to 2D either asymptotically at $N = \infty$ or critically at some finite width N_c. Notice that this change of dimensional characteristics occurs purely due to a critical change of lattice topology, different from those caused by the variation of temperature or spin-spin coupling anisotropy [7–10]. To the best of our knowledge, there is no report in the literature of a finite N_c at which the dimensional transition takes place. Namely, the continuous spin-rotational symmetry may break spontaneously at N_c. Existing qualitative theories of spontaneous continuous symmetry breaking have not explicitly considered such a delicate case.

On one hand, the Mermin-Wagner theorem [11,12] states that the Heisenberg model cannot have spontaneous ordering at any finite temperature in both 1D and 2D. For GS, despite the possible failure [13], the quantum-classical mapping is used to show that the Heisenberg model supports spontaneous ordering in 2D. It is stated [14] that the GS in a 1D quantum spin system is a critical point for Mermin-Wagner theorem. So far, no spontaneous magnetic order is found for a purely 1D spin-$\frac{1}{2}$ antiferromagnetic chain. However, the spontaneous long-range order exists in a 1D chain which is not so pure as to include unequal spins [14,15]. On the other hand, the long-range order is considered via a variety of inequalities. The early significant representative of this kind is the work of Dyson, Lieb, and Simon (DLS) [16]. Later, there emerged the usage of Duhamel two-point function in the inequality theory [17]. The inequality theory is used to investigate higher dimensions first, i.e., from three dimensions [17–19] to multilayer [20] and from high spin [21] to low spin, etc. There is no rigorous result for the GS of a 2D spin-$\frac{1}{2}$ square lattice yet. It is worth noting the inequality theory showed [22] that a spin chain with power-law decaying long-range coupling may or may not have spontaneous ordering depending on the decaying rate. Nonetheless, neither the Mermin-Wagner theorem nor the inequality theory has considered the general case of an $\infty \times N$ lattice. This prompts some natural questions: When an $\infty \times N$ square lattice is viewed as an effective 1D lattice whose element is a ladder rung, does its

*wanglihua94@tsinghua.org.cn
†kim@unist.ac.kr

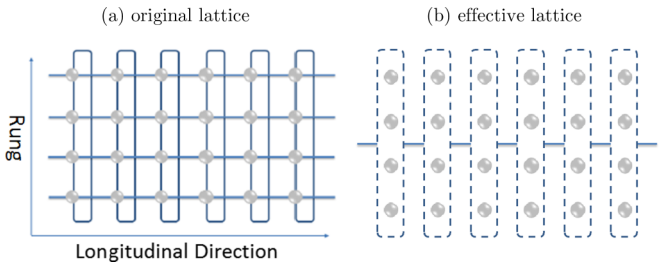

FIG. 1. Spin-$\frac{1}{2}$ antiferromagnetic Heisenberg model on an $\infty \times N$ ladder ($N = 4$ for example). The circle represents lattice sites, and the lines and curves connecting the nearest-neighboring sites represent the spin-spin interactions. Periodic boundary conditions are assumed. (a) The original lattice. (b) The effective lattice whose single site is indicated by the dashed rectangle enclosing the N lattice sites in each rung of original lattice.

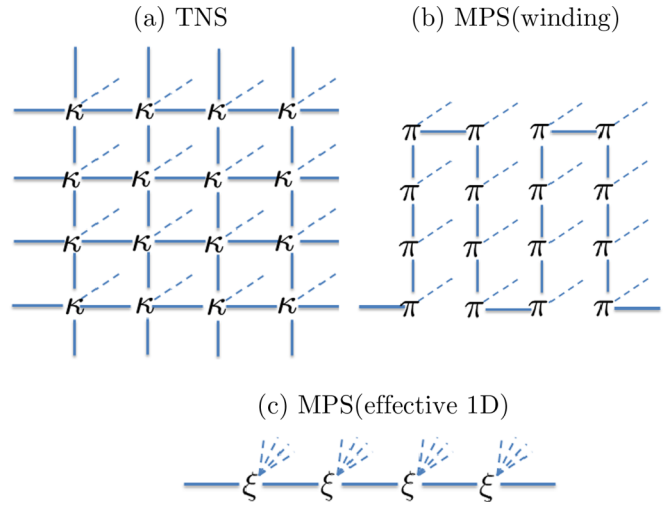

FIG. 2. Various designs for the lattice wave function using tensor/matrix product. ξ denotes a tensor. The solid line refers to the bonding index while the dashed line refers to the space index. (a) Tensor network state (TNS). Each tensor has four bonding indices which resemble the same lattice architecture shown in Fig. 1 and one space index which accounts for a lattice site. TNS is employed in iPEPS, etc. (b) Matrix product state (MPS) built on a winding lattice chain. Each tensor has two bonding indices that differ from the lattice-linking architecture and one space index for a site. DMRG wave function after projections are reduced to this form of MPS. (c) MPS built on a lattice chain of a translational symmetry. The two bonding indices resemble the architecture of an effective lattice shown in Fig. 1(b); the combination of dashed lines, each of which corresponds to a physical site of each ξ, is treated as a single space index running from 1 to 2^N for spin-$\frac{1}{2}$.

GS support the spontaneous ordering? Does the value of N matter?

The nonlinear sigma model (NLSM) has its own answer to those questions, in a semiquantitative way [23,24] which we found arguable. It predicts [25,26] that the physics of a spin ladder can only qualitatively change at $N = \infty$ and the energy gap of a ladder closes up exponentially with its width N. But the perturbative nature of mapping the spin-$\frac{1}{2}$ ladder to NLSM necessarily indicates a threshold value of the gap beyond which the perturbation would be inapplicable. In fact, its prediction of the gap was numerically checked only for $M \times N$ lattices with $M \gg N$ and N up to 6 [27,28]. And, the latest size scaling of $N \times N$ or $M \times N$ lattices in the literature did not handle larger N yet and hence did not capture any dimensional transition [29,30] though the possibility is not excluded [31]. Therefore, it is worth numerically exploring the possibility of such a quantum dimensional transition at finite N for a true $\infty \times N$ lattice of larger N's, by monitoring the emerging order parameters such as the stagger magnetization and the spin-spin correlation at infinite separation. The model Hamiltonian is

$$H = J \sum_{\lceil (i,j),(i',j') \rceil} \vec{S}_{(i,j)} \cdot \vec{S}_{(i',j')}, \tag{1}$$

where $\vec{S}_{(i,j)}$ is the spin vector operator on the (i, j)th lattice site with i running from $-\infty$ to ∞ in the longitudinal direction (LD) and j running from 1 to N in the rung. $\lceil \ldots \rceil$ sums over the nearest-neighboring sites. J is the spin-spin coupling integral and is normalized to 1 hereafter. The periodic boundary condition (PBC) is assumed in both directions. See Fig. 1(a) for the schematic of the lattice geometry and interaction configurations.

There are some other analytic methods for this model. None of them have clarified the spontaneous symmetry breaking in the model studied here. Bethe ansatz [3] only works for $N = 1$. Bosonization [32,33] predicts a power-law decay of the spin-spin correlation $C(r) \equiv \langle S^z_{(i,1)} S^z_{(i+r,1)} \rangle \propto r^{-1}$ for $N = 1$, r being the spin-spin separation. Conformal field theory (CFT) [34,35] further predicts a logarithmic correction multiplying with the power function, which was confirmed [36] to be asymptotically effective after 1000 lattice separations. CFT [37] also gives a solution in limiting cases for $N > 1$ such as the 2D Ornstein-Zernike form of spin-spin correlations for weakly coupled spin ladders. The spin-wave theory (SWT) [38,39] essentially provides an approximation in the continuum limit and assumes the magnon excitation, excluding the spinon excitation, hence making no decisive claim on the quantum dimensional transition.

On the numerical side, it is not feasible for stochastic methods such as Monte Carlo method [40] which otherwise is powerful in searching energy of a finite system. Finite $M \times N$ lattices, with $M \gg N$, were simulated [5], trying to scale away the finite-size effect. A similar finite lattice was also simulated [30] by the density matrix renormalization group method (DMRG) [41,42]. But, sweeping an $\infty \times N$ lattice to establish long-range spin-spin correlations for large N is not yet practical. Variants of DMRG such as infinite time evolving block decimation (iTEBD) method were applied to the case of $N = 2$ [43], yielding results conflicting with that by the infinite quasi-1D entanglement perturbation theory (iqEPT) [44], and so on [45], but not for larger N because of the rapid increase of the number of density matrix elements needed for a sufficient accuracy. Tensor network state (TNS) [46,47] based methods such as the infinite projected entangled pair state (iPEPS) [48,49], illustrated in Fig. 2(a) and natively designed for an infinite 2D system still do not show sufficient efficiency to tackle the tensor's bond index size greater than a few dozen [49,50]. This hinders its application to investigate

the very fine structure of the spin-spin correlation covering large separations within large systems [51]. Nevertheless, understanding the dimensional transition is important in taking the right numerical strategy to deal with strong correlation in a low-dimensional quantum system. For instance, DMRG works extremely well in 1D but not in 2D. When dealing with a 2D lattice, the wave function obtained in DMRG has a matrix product state (MPS) [36,52–60] form that is built on a wound 1D lattice which resembles the 2D lattice [29,50]. See Fig. 2(b) for an illustration. According to the area law [61], the required MPS rank (bond index size) characterizing the entanglement in the wave function increases too rapidly in this way [62]. Rather than treating the $\infty \times N$ lattice as a wound 1D lattice, it can also be treated as a 1D lattice by converting N physical sites in each rung into an effective site [44] [Fig. 1(b)]. We take the latter approach in this study and use the $\infty \times N$ lattice to investigate if the system wave function, no matter which dimensional characteristics its GS turns out to have, can be universally represented by the MPS whose bonding topology is the same as the lattice linking architecture [compare the effective lattice structure in Fig. 1(b) and the MPS structure in Fig. 2(c)]. Hence, we suppress the increase of MPS rank with N to a manageable rate.

We organize the remainder of the discussion as follows. We first discuss our numerical method in Sec. II. Section II A is dedicated to the parametrized matrix product operator (MPO) [36,44,56,57,59,62–64] for an $\infty \times N$ spin-$\frac{1}{2}$ antiferromagnetic Heisenberg model; Sec. II B to the variation of MPS in the presence of MPO; Secs. II C and II D to entanglement perturbation of MPO and of Hilbert space, respectively; Sec. II E to implementation of the antiferromagnetic checkerboard symmetry; Sec. II F to integration of the Davidson eigenvalue solver with MPS and MPO; Sec. II G to the space reduction in MPS; Sec. II H to a useful relationship between the spin-spin correlations and the staggered magnetization. There, we also demonstrate that $\ln(\ln C_r - \ln C_{r+1})$, C_r being the spin-spin correlation at separation r, can be used to interpret order and disorder. Next, benchmarks on decoupled ladders and ladders with open boundary condition in the rung are given in Sec. III. It is followed by Sec. IV for the GS properties of the target model, i.e., the ladder with periodic boundary condition in the rung, including the signature of a dimensional transition at $N_c = 10$. The conclusion is stated in Sec. V and an outlook is given in Sec. VI.

II. METHOD: INFINITE QUASI-1D ENTANGLEMENT PERTURBATION THEORY

We developed a numerical method called infinite quasi-1D entanglement perturbation theory (iqEPT). We divide an $\infty \times N$ square lattice into an infinite chain of effective sites, each of which is converted from the N sites in the rung. See Fig. 1(b) for illustration. The wave function is written in a MPS that is built on the effective sites. Meanwhile, the Hamiltonian H is transformed to a MPO via the density operator $e^{-\beta H}$ with β being a small positive constant [36,44,55,56]. Varying $\langle e^{-\beta H}\rangle$ with respect to the MPS tensor yields a generalized eigenvalue equation (GEE). The GEE is formed using the trial MPS wave function at the very beginning and then is updated by the solved eigenvector corresponding to the largest eigenvalue at each iteration. Eventually, the eigenvector approaches the fixed state for a given rank P. Adding small elements to the obtained MPS matrix ranked at P to form a trial MPS matrix ranked slightly larger at $P + \Delta P$, we carry on the previous process until convergence is reached. Thus, those obtained quantities will converge with P. The final largest eigenvalue, i.e., $e^{-\beta\epsilon_0}$, gives the GS energy ϵ_0.

The essential concept that distinguishes iqEPT from other MPS methods is that it expresses the Hamiltonian as a parametrized MPO [36,55,56] and this parameter was used to reduce the linking complexity between the building units of MPO [44]. In this work, we further point out that it is equivalent to treat the entanglement in MPO in perturbation, as will be explained in Sec. II C. The rank (bond index size) of a MPO tensor is reduced to $3N + 1$ from the original scale of 4^N. We also integrate the Jacobi-Davidson method for GEE [65] with both MPO and MPS, without explicitly forming GEE. The details are given in Sec. II F. As a result, we were able to handle the unprecedented GEE rank as large as $2^{14} \times 350^2 = 2.0 \times 10^9$ with $P = 350$ for $N = 14$.

A. Parametrized matrix product operator for an $\infty \times N$ square lattice

In what follows, the Einstein summation convention is implied for repeating indices in a formula except stated otherwise. $(x \leftrightarrow y)$ denotes pairing between two physical sites x and y. $\lfloor \alpha_1, \ldots, \alpha_m \rfloor$ combines m individual indices $\alpha_1 = 1, \ldots k_1, \ldots, \alpha_m = 1, \ldots, k_m$ into a single flattened index $\alpha = 1, \ldots, \prod_i^m k_i$.

After the physical sites in each rung are converted as a single effective site, the Hamiltonian is further rewritten as

$$H = \sum_{\{a,b\}} (H_a + H_b), \tag{2}$$

where the summation runs over the two sets of bonds, $\{a\}$ and $\{b\}$, between nearest-neighboring physical sites. If the two physical sites of a bond reside on different effective sites, it is collected in the inter-effective-site set $\{a\}$, and otherwise in the intra-effective-site set $\{b\}$. Figure 3 illustrates various bonds in the case of $N = 4$. In this case, each effective site, say the ith site, has four intra-effective-site bonds b_1^i, b_2^i, b_3^i, and b_4^i. It also participates in eight inter-effective-site bonds. The first four are labeled with index $i - 1$: a_1^{i-1}, a_2^{i-1}, a_3^{i-1}, and a_4^{i-1}. They bond physical sites residing on the $(i-1)$th and ith effective sites. The last four are labeled with index i; they are a_1^i, a_2^i, a_3^i, and a_4^i bonding physical sites residing on the ith and $(i+1)$th effective sites. These sets of bonds are used to rewrite the Hamiltonian as

$$e^{-\beta H} \approx \prod_i \left(\prod_k e^{-\beta H_{a_k^i}} \prod_l e^{-\beta H_{b_l^i}} \right) + O(\beta^2), \tag{3}$$

where $i = 1, \ldots, \infty$ and $k, l = 1, \ldots, N$. Although the sequence of the bonds grouped as the single exponent in the left-hand side of Eq. (2) does not matter, it matters in the right-hand side in that the ordering of i, k, l is equivalent to permuting the Hamiltonian matrix. The permutation does

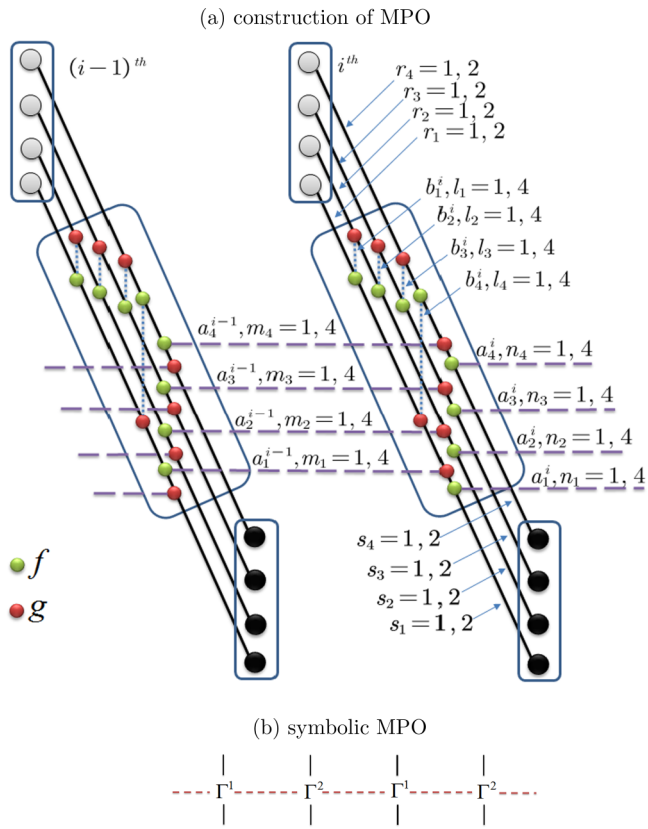

FIG. 3. Illustration of MPO for $N = 4$. (a) The construction. The local quantum space is represented by rectangles enclosing four physical sites (circle in gray color). Directed out of the page is the conjugate of those spaces. The building units of MPO, symbolized by Γ^1 and Γ^2 in (b), are enclosed within the tilted rectangles in-between the spaces. Going from the space to its conjugate, the first four pairs of green-red solid circles are stacked shell by shell in sequence. They account for the on-effective-site interaction, with the green/red circle denoting f/g operator mentioned in the context. The dashed line denotes the contraction of bond index running from 1 to 4. The solid line denotes the inner product between the operators operating sequentially on the same physical lattice site. Following the on-effective-site operators are one shell of f/g operators bonding the $(i-1)$th/ith effective sites, and another shell of g/f operators bonding the $(i-2)$th/$(i-1)$th effective sites and the ith/$(i+1)$th effective sites, respectively. They are stacked layer by layer from bottom to top, forming inter-effective-site interactions and hence giving the rise of entanglement in MPO represented schematically by the horizontal dashed lines in (b). The individual space indices $r_{i=1,4}/s_{i=1,4}$ are combined into single indices of vertical solid lines in (b), while the individual bond indices $m_{i=1,4}/n_{i=1,4}$ being combined into horizontal dashed lines in (b).

not affect the physical property but requires the corresponding linear manipulation of the representation basis. We choose to operate $\prod_k e^{-\beta H_{a_k^i}}$ on $\prod_l e^{-\beta H_{b_l^i}}$ for given i. A physical site of the ith effective site is denoted as x^i, $x = 1, \ldots, N$, from bottom to top in the rung. For the set $\{b_l^i\}$, it is ordered such that $l = 1 : (1^i \leftrightarrow 2^i)$, $2 : (2^i \leftrightarrow 3^i)$, $\ldots$, $N : (N^i \leftrightarrow 1^i)$. For the set $\{a_k^i\}$, it is ordered such that $k = 1 : (1^i \leftrightarrow 1^{i+1})$, $2 : (2^i \leftrightarrow 2^{i+1})$, $\ldots$, $N : (N^i \leftrightarrow N^{i+1})$. It is clear that the successive product of $e^{-\beta H_{b_l^i}}$ involves only one effective site. The N operations are stacked in a shell-by-shell manner in and out of the page. It is followed by the successive product of $e^{-\beta H_{a_k^i}}$ which operates on the physical sites across two effective sites. They are stacked from bottom to top in a layer-by-layer manner. See Fig. 3 for details. Each individual density operator for a general bond $(i \leftrightarrow j)$ in the right-hand side of Eq. (3) is Taylor expanded as, utilizing small positive β,

$$e^{-\beta(S_i^x S_j^x + S_i^y S_j^y + S_i^z S_j^z)} \approx I - \beta\left(S_i^x S_j^x + S_i^y S_j^y + S_i^z S_j^z\right) \equiv f_\alpha \otimes g_\alpha. \tag{4}$$

$f_{\alpha=1,4}$ operating on the first physical site of a bond are 2×2 matrices (identity, $\sqrt{\beta}S^x$, $\sqrt{\beta}\bar{S}^y$, and $\sqrt{\beta}S^z$); $g_{\alpha=1,4}$ operating on the second physical site are 2×2 matrices (identity, $-\sqrt{\beta}S^x$, $\sqrt{\beta}\bar{S}^y$, and $-\sqrt{\beta}S^z$). Note that g's differ from f's in that the former has the minus sign; $\bar{S}_i^y \otimes \bar{S}_j^y = -S_i^y \otimes S_j^y$ with $\bar{S}^y = \left(\begin{smallmatrix} 0 & -1 \\ 1 & 0 \end{smallmatrix}\right)$ being a real version of S^y to avoid any complex element in the matrix.

Now consider the product of two individual density operators of two bonds c and c'. There follow two rules applied in different cases. Rule A: $e^{-\beta H_c} e^{-\beta H_{c'}} = f_\alpha \otimes g_\alpha \otimes f_\gamma \otimes g_\gamma$ if there is no shared physical site. Rule B: $e^{-\beta H_c} e^{-\beta H_{c'}} = f_\alpha \otimes (g_\alpha \cdot f_\gamma) \otimes g_\gamma$ if there is a shared physical site.

Rule A is transparent. The formula shown in Rule B applies to the case where the shared site is the first site of bond c' and the second site of bond c. Nevertheless, the combination of shared site positions respectively in c and c' is diverse, such as first vs first, second vs second, etc. They all appear in Fig. 3. The formula in Rule B will be slightly adjusted accordingly.

After applying these rules, the density operator involving the ith effective site is

$$\begin{aligned}\left(f_{n_1} \cdot g_{m_1} \cdot g_{l_4} \cdot f_{l_1}\right) &\otimes \left(f_{n_2} \cdot g_{m_2} \cdot f_{l_2} \cdot g_{l_1}\right) \\ &\otimes \left(f_{n_3} \cdot g_{m_3} \cdot f_{l_3} \cdot g_{l_2}\right) \\ &\otimes \left(f_{n_4} \cdot g_{m_4} \cdot f_{l_4} \cdot g_{l_3}\right).\end{aligned} \tag{5}$$

Each of the indices of bond set $\{b^i\}$, l_1, l_2, l_3, and l_4, appears twice in expression (5), implying self-contraction of intra-effective-bonds. The uncontracted indices m_1, m_2, m_3, and m_4 entangle the ith effective site with the $(i-1)$th effective site through the bond set $\{a^{i-1}\}$; the other uncontracted indices n_1, n_2, n_3, and n_4 entangle the ith effective site with the $(i+1)$th effective site through the bond set $\{a^i\}$. In fact, fixing indices m's and n's to $\{m\}_0$ and $\{n\}_0$, each resultant quantity in every set of parentheses of (5) is a local density matrix (ρ_{r_u,s_u}). $u = 1, \ldots, 4$ refer to the four sets of parentheses. Each of r's or s's runs from 1 to 2 accounting for spin-$\frac{1}{2}$. The combinations $r^i \equiv \lfloor r_1, r_2, r_3, r_4 \rfloor$ and $s^i \equiv \lfloor s_1, s_2, s_3, s_4 \rfloor$ run from 1 to 2^N. The direct product between the four local density matrices spans a resultant density matrix $\Gamma_{r^i s^i, \{m\}_0\{n\}_0}$ of rank of 2^N for the ith effective site. Allowing m's and n's to vary, Γ becomes a four-legged tensor $\Gamma_{r^i s^i, mn}$. The combinations $m \equiv \lfloor m_1, m_2, m_3, m_4 \rfloor$ and $n \equiv \lfloor n_1, n_2, n_3, n_4 \rfloor$ are the bond indices and run from 1 to 4^N. Considering the bipartite structure due to the antiferromagnetic nature, Eq. (3)

is transformed to a parametrized MPO as follows:

$$e^{-\beta H} = \sum_{\substack{\dots r^{i-1} r^{i} \dots \\ \dots s^{i-1} s^{i} \dots}} \mathrm{tr}\big(\dots \Gamma^{1}_{r^{i-1}s^{i-1},mn}(\beta)\Gamma^{2}_{r^{i}s^{i},no}(\beta)\dots\big) \times \dots \big|\phi^{i-1}_{r^{i-1}}\big\rangle\big\langle\phi^{i}_{r^{i}}\big| \dots \big\langle\phi^{i-1}_{s^{i-1}}\big|\big\langle\phi^{i}_{s^{i}}\big| \dots . \tag{6}$$

Note that in Eqs. (3) and (6), the small parameter β is used to express $e^{-\beta H}$ as a successive product of operators according to Baker-Campbell-Hausdorff (BCH) formula, implying that parts of high-order terms in β are already neglected controllably. Nevertheless, many other high-order terms in β still remain in the operator, which is a consistency check of formula (5). We will show in Sec. II C that the remaining high-order terms in β could be treated perturbatively to reduce the last two (bond) indices of $\Gamma^{1,2}$ from 4^N to $3N+1$. But, for the moment, we first discuss how to variationally optimize the MPS wave function in the presence of MPO.

B. Variational optimization of MPS in the presence of MPO

The system wave function is expressed as a MPS

$$|\Psi\rangle = \sum_{\dots r^{i-1} r^{i} \dots} \mathrm{tr}\big(\dots \xi^{1}_{r^{i-1}} \cdot \xi^{2}_{r^{i}} \dots\big) \dots \big|\phi^{i-1}_{r^{i-1}}\big\rangle\big|\phi^{i}_{r^{i}}\big\rangle \dots, \tag{7}$$

which has the $\xi^{1,2}$ repetition structure, similar to that for MPO, due to the antiferromagnetic condition. Note that $\xi^{1,2}$ are three-legged tensors. For example, $\xi^{2}_{r^{i}}$ for the ith effective site is explicitly denoted with the index of the first leg, $r^{i} = 1, 2, \dots, 2^{N}$, which refers to the local quantum state $|\phi^{i}_{r^{i}}\rangle$. Explicitly writing the other two legs m and n in $\xi^{2}_{r^{i},mn}$ are the left and right indices of a matrix, fixing r^{i}. Therefore, each of $\xi^{1,2}$ has $2^{N}P^{2}$ variables when the matrix rank is P. Given a configuration (Fock vector) of the local state of all effective sites, a specific $P \times P$ matrix is then assigned to each effective site; the left and right indices of that matrix contract in a closed form with the right and left indices of the matrix of the front and rear effective sites to yield a trace-out. The resultant scalar value is the superposition coefficient of the configuration in the wave function. Optimization of the wave function by pinpointing the superposition coefficient is equivalent to optimization of those $P \times P$ matrices, 2×2^{N} matrix elements in total, in the MPS with the bipartition structure.

The MPS matrices can be optimized in various ways. One way used in DMRG is to start with an exact solution of a small part of system and then to renormalize the representation basis every time the new parts interacting with the processed part are added. The MPS matrix is a fixed point after many projections of the DMRG solution [62]. The other way is to vary the energy observation with respect to the MPS matrices, hence, to optimize them simultaneously. Illustrated in Fig. 4, the energy observation is expressed as

$$\begin{aligned}\langle\psi|e^{-\beta H}|\psi\rangle = &\left[\sum_{\dots s^{i-1}s^{i}\dots} \mathrm{tr}\big(\dots \xi^{1}_{s^{i-1},\alpha_1\gamma_1}\xi^{2}_{s^{i},\gamma_1\eta_1}\dots\big)\dots\big\langle\phi^{i-1}_{s^{i-1}}\big|\big\langle\phi^{i}_{s^{i}}\big|\dots\right]\left[\sum_{\dots r^{i-1}r^{i}\dots} \mathrm{tr}\big(\dots \xi^{1}_{r^{i-1},\alpha_3\gamma_3}\xi^{2}_{r^{i},\gamma_3\eta_3}\dots\big)\dots\big|\phi^{i-1}_{r^{i-1}}\big\rangle\big|\phi^{i}_{r^{i}}\big\rangle\dots\right] \\ &\times\left[\sum_{\substack{\dots z^{i-1}z^{i}\dots \\ \dots w^{i-1}w^{i}\dots}} \mathrm{tr}\big(\dots \Gamma^{1}_{z^{i-1}w^{i-1},\alpha_2\gamma_2}\Gamma^{2}_{z^{i}w^{i},\gamma_2\eta_2}\dots\big)\dots\big|\phi^{i-1}_{z^{i-1}}\big\rangle\big|\phi^{i}_{z^{i}}\big\rangle\dots\big\langle\phi^{i-1}_{w^{i-1}}\big|\big\langle\phi^{i}_{w^{i}}\big|\dots\right] \\ &= \mathrm{tr}(\dots A_{\alpha\gamma}B_{\gamma\eta}\dots),\end{aligned} \tag{8}$$

where the Kronecker delta function $\langle\phi^{i}_{s^{i}}|\phi^{i}_{z^{i}}\rangle = \delta_{s^{i},z^{i}}$, etc., is used to reduce the summations. And, we have

$$A_{\alpha\equiv\lfloor\alpha_1\alpha_2\alpha_3\rfloor,\gamma\equiv\lfloor\gamma_1\gamma_2\gamma_3\rfloor} \equiv \xi^{1}_{s^{i-1},\alpha_1\gamma_1}\Gamma^{1}_{s^{i-1}r^{i-1},\alpha_2\gamma_2}\xi^{1}_{r^{i-1},\alpha_3\gamma_3}, \quad B_{\gamma\equiv\lfloor\gamma_1\gamma_2\gamma_3\rfloor,\eta\equiv\lfloor\eta_1\eta_2\eta_3\rfloor} \equiv \xi^{2}_{s^{i},\gamma_1\eta_1}\Gamma^{2}_{s^{i}r^{i},\gamma_2\eta_2}\xi^{2}_{r^{i},\gamma_3\eta_3}. \tag{9}$$

$\alpha \equiv \lfloor\alpha_1\alpha_2\alpha_3\rfloor$ denotes the combination of indices $\alpha_1, \alpha_3 = 1, 2, \dots, P$ (P is a given MPS rank) and $\alpha_2 = 1, 2, \dots, 4^{N}$, giving rise to a single index $\alpha = 1, 2, \dots, 4^{N}P^{2}$, etc. Meanwhile, the normalization factor is

$$\begin{aligned}\langle\psi|\psi\rangle = &\left[\sum_{\dots s^{i-1}s^{i}\dots} \mathrm{tr}\big(\dots \xi^{1}_{s^{i-1},\alpha_1\gamma_1}\xi^{2}_{s^{i},\gamma_1\eta_1}\dots\big)\dots\big\langle\phi^{i-1}_{s^{i-1}}\big|\big\langle\phi^{i}_{s^{i}}\big|\dots\right]\left[\sum_{\dots r^{i-1}r^{i}\dots} \mathrm{tr}\big(\dots \xi^{1}_{r^{i-1},\alpha_3\gamma_3}\xi^{2}_{r^{i},\gamma_3\eta_3}\dots\big)\dots\big|\phi^{i-1}_{r^{i-1}}\big\rangle\big|\phi^{i}_{r^{i}}\big\rangle\dots\right] \\ &= \mathrm{tr}\big(\dots C_{\alpha\gamma}D_{\gamma\eta}\dots\big).\end{aligned} \tag{10}$$

Matrices C and D are formed as

$$\begin{aligned}C_{\alpha\equiv\lfloor\alpha_1\alpha_3\rfloor,\gamma\equiv\lfloor\gamma_1\gamma_3\rfloor} &\equiv \xi^{1}_{r^{i-1},\alpha_1\gamma_1}\xi^{1}_{r^{i-1},\alpha_3\gamma_3}, \\ D_{\gamma\equiv\lfloor\gamma_1\gamma_3\rfloor,\eta\equiv\lfloor\eta_1\eta_3\rfloor} &\equiv \xi^{2}_{r^{i},\gamma_1\eta_1}\xi^{2}_{r^{i},\gamma_3\eta_3},\end{aligned} \tag{11}$$

where the combination of indices $\alpha_1, \alpha_3 = 1, 2, \dots, P$ gives rise to a single index $\alpha = 1, 2, \dots, P^{2}$, etc. Equation (8) is rewritten as

$$\langle e^{-\beta H}\rangle = \frac{\langle\psi|e^{-\beta H}|\psi\rangle}{\langle\psi|\psi\rangle} = \lim_{M\to\infty}\frac{\mathrm{tr}(AB)^{M}}{\mathrm{tr}(CD)^{M}}. \tag{12}$$

Then, the first derivative of $\langle e^{-\beta H}\rangle$ with respect to $\xi^{1,2}$, say ξ^{1}, leads to

$$\frac{\partial\langle\psi|e^{-\beta H}|\psi\rangle}{\partial\xi^{1}} = \langle e^{-\beta H}\rangle\frac{\partial\langle\psi|\psi\rangle}{\partial\xi^{1}}. \tag{13}$$

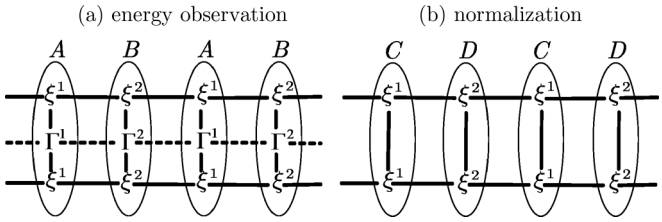

FIG. 4. (a) Energy observation in the presence of MPS and MPO. The quantities enclosed in each ellipse are combined into new tensors A and B, each of which has a larger rank of P^2Q with P and Q being the MPS and MPO ranks, respectively. (b) Normalization of MPS wave function. The quantities enclosed in each ellipse are combined into new tensors C and D, each of which has a rank of P^2.

Substituting the numerator and denominator in the right-hand side of Eq. (12) into both sides of Eq. (13), respectively, we arrive at

$$\mathrm{tr}\left[(AB)^{M-1}\frac{\partial A}{\partial \xi^1}B\right] = \langle e^{-\beta H}\rangle \mathrm{tr}\left[(CD)^{M-1}\frac{\partial C}{\partial \xi^1}D\right]. \tag{14}$$

By singular-value decomposition (SVD) of the building units in Eq. (12), we have

$$\begin{aligned} AB &= u\Lambda v, \\ CD &= u'\Delta v'. \end{aligned} \tag{15}$$

Substituting Eq. (15) into (14) derives that

$$v\frac{\partial A}{\partial \xi^1}Bu = \langle e^{-\beta H}\rangle\left(\frac{\Delta_1}{\Lambda_1}\right)^{M-1} v'\frac{\partial C}{\partial \xi^1}Du'. \tag{16}$$

In the above, only the largest eigenvalues Λ_1 (Δ_1) and the corresponding right (left) eigenvectors v/u (v/u') survive when $M \to \infty$. On the other hand, substituting Eq. (15) into (12) leads to

$$\langle e^{-\beta H}\rangle^{\frac{1}{M}} = \frac{\Lambda_1}{\Delta_1}. \tag{17}$$

Substituting Eq. (17) into (16), we arrive at

$$v\frac{\partial A}{\partial \xi^1}Bu = \langle e^{-\beta H}\rangle^{\frac{1}{M}} v'\frac{\partial C}{\partial \xi^1}Du'. \tag{18}$$

In fact, Eq. (18) is a generalized eigenvalue equation (GEE). To confirm it, it is instructive to explicitly rewrite both sides as

$$\begin{aligned} v\frac{\partial A}{\partial \xi^1}Bu &= X_{\lfloor r^{i-1},\alpha_1,\gamma_1\rfloor,\lfloor s^{i-1},\alpha_3,\gamma_3\rfloor}\chi^1_{\lfloor s^{i-1},\alpha_3,\gamma_3\rfloor} = X\chi^1, \\ v'\frac{\partial C}{\partial \xi^1}Du' &= Y_{\lfloor r^{i-1},\alpha_1,\gamma_1\rfloor,\lfloor s^{i-1},\alpha_3,\gamma_3\rfloor}\chi^1_{\lfloor s^{i-1},\alpha_3,\gamma_3\rfloor} = Y\chi^1, \end{aligned} \tag{19}$$

where $\chi^1_{\lfloor s^{i-1},\alpha_3,\gamma_3\rfloor}$ is the vector version of three-leg tensor $\xi^1_{s^{i-1},\alpha_3\gamma_3}$. In addition,

$$\begin{aligned} &X_{\lfloor r^{i-1},\alpha_1,\gamma_1\rfloor,\lfloor s^{i-1},\alpha_3,\gamma_3\rfloor} \\ &\quad = v_{\alpha_1\alpha_2\alpha_3}\Gamma^1_{r^{i-1}s^{i-1},\alpha_2\gamma_2}\xi^2_{r^i,\gamma_1\eta_1}\Gamma^2_{r^is^i,\gamma_2\eta_2}\xi^2_{s^i,\gamma_3\eta_3}u_{\eta_1\eta_2\eta_3}, \\ &Y_{\lfloor r^{i-1},\alpha_1,\gamma_1\rfloor,\lfloor s^{i-1},\alpha_3,\gamma_3\rfloor} \\ &\quad = v'_{\alpha_1\alpha_3}\delta_{r^{i-1},s^{i-1}}\xi^2_{r^i,\gamma_1\eta_1}\xi^2_{r^i,\gamma_3\eta_3}u'_{\eta_1\eta_3} \end{aligned} \tag{20}$$

are matrices. Thus, we have

$$\begin{aligned} X\chi^1 &= \langle e^{-\beta H}\rangle^{\frac{1}{M}} Y\chi^1, \\ X'\chi^2 &= \langle e^{-\beta H}\rangle^{\frac{1}{M}} Y'\chi^2, \end{aligned} \tag{21}$$

where another generalized eigenvalue equation is generated for χ^2, the vector version of the three-leg tensor ξ^2. It is straightforward that X/X' and Y/Y' are functionals of χ^2/χ^1. If we start to generate the GEEs with the trial vectors $\chi^{1,2}_{0,P_0}$, the rank of each being as small as $2^N P_0^2$, a new set of vectors $\chi^{1,2}_{1,P_0}$ are obtained by solving those GEEs and are used to update the GEEs. Iterations are carried on until the norm of $\|\chi^{1,2}_{m+1,P_0} - \chi^{1,2}_{m,P_0}\|$ is less than a threshold value. The converged vectors for P_0 are used to generate the trial vectors for a slightly larger rank $P_0 + \Delta P$ by adding small new elements to the enlarged vectors. A second type of convergence with respect to P should eventually bring the identical largest eigenvalue $\lambda = \frac{\Lambda_1}{\Delta_1}$ for Eq. (21). We have

$$\langle e^{-\beta H}\rangle = \lambda^M. \tag{22}$$

The GS energy of an $\infty \times N$ lattice is

$$\epsilon_0 = -\beta^{-1}\ln\langle e^{-\beta H}\rangle = -M\beta^{-1}\ln\lambda. \tag{23}$$

The GS energy per spin is

$$\bar{\epsilon}_0 = \frac{\epsilon_0}{2MN} = -(2N\beta)^{-1}\ln\lambda. \tag{24}$$

C. Entanglement perturbation in Hamiltonian space

There are two kinds of eigenvalue equations to be solved in this method. The first kind is the SVDs in Eq. (15) for the left and right eigenvectors of two asymmetric matrices. The first matrix has rank $R_1 = 4^N P^2$ while the second has rank $R'_1 = P^2$; the second kind is the GEEs in Eq. (21) of rank $R_2 = 2^N P^2$. It is obvious that R_1 dominates R_2 when $N > 1$. The largest simulation scale in our study is for $N = 14$ and $P = 350$. It corresponds to $R_1 = 3.3 \times 10^{13}$ and demands 30 TB memory to store even a single eigenvector, not to mention that solving an eigenvalue equation requires much more memory allocation than that merely to store a single eigenvector. This data scale is apparently not practical for modern computers.

Fortunately, there is a simple way to overcome this difficulty. Examining $f_{\alpha=1,\ldots,4}$ and $g_{\alpha=1,\ldots,4}$, the $\alpha = 1$ terms are the identity matrix, zeroth order in β; the terms of $\alpha = 2, 3, 4$ are all in the order of $\sqrt{\beta}$. But, whenever there is a term of order $\sqrt{\beta}$, there should be a counterpart in the same order at the other end of a bond. They actually generate terms in the first order of β. On the other hand, according to formula (5), the bond index of $\Gamma^{1,2}$, say, $m \equiv \lfloor m_1, \ldots, m_N\rfloor$, is a combination of $m_1, \ldots, m_N$, each of which is the index of f or g running from 1 to 4. Because $\beta \leqslant 10^{-7}$, it is safe to discard the terms in the order of β^2 and beyond. Therefore, it amounts to keeping, among 4^N combinations of $\lfloor m_1, \ldots, m_N\rfloor$, those terms with at most one of m's not being 1. The new bond index of $\Gamma^{1,2}$, after reduction, now runs from 1 to $3N + 1$ instead from 1 to 4^N. In the case of $N = 4$, they are 1 for 1111, 2 for 1112, 3 for 1113, 4 for 1114, 5 for 1121, 6 for 1131, etc.

At this point, we reduced the rank of MPO tensor by rewriting it in terms of a perturbative expansion in the small positive parameter β. Now, we show that the reduction of rank corresponds to the entanglement reduction in MPO. The MPO is an entangled quantity in that it cannot be expressed as the product of individual multiplicative quantities that is associated with local quanta, namely, the local state of the effective site in this study.

Like the Hilbert space for the wave function of a quantum lattice $\cdots \otimes \{|\phi_i\rangle\} \otimes \{|\phi_{i+1}\rangle\} \otimes \cdots$, we define a space $\mathfrak{H}$, $\cdots \otimes \{|\phi_i\rangle\langle\phi'_i|\} \otimes \{|\phi_{i+1}\rangle\langle\phi'_{i+1}|\} \otimes \cdots$, for the Hamiltonian. It is not hard to show that it is indeed a vector space after defining an inner product, i.e., vector-vector multiplication as

$$\begin{aligned}
&\vec{h}_1 \cdot \vec{h}_2 \\
&= \ldots (\langle\varphi'_i|\phi_i\rangle\langle\phi'_i|\varphi_i\rangle)(\langle\varphi'_{i+1}|\phi_{i+1}\rangle\langle\phi'_{i+1}|\varphi_{i+1}\rangle)\ldots \\
&\quad \forall\, \vec{h}_1, \vec{h}_2 \in \mathfrak{H} \\
&\vec{h}_1 = \cdots \otimes \{|\phi_i\rangle\langle\phi'_i|\} \otimes \{|\phi_{i+1}\rangle\langle\phi'_{i+1}|\} \otimes \cdots, \\
&\vec{h}_2 = \cdots \otimes \{|\varphi_i\rangle\langle\varphi'_i|\} \otimes \{|\varphi_{i+1}\rangle\langle\varphi'_{i+1}|\} \otimes \cdots. \qquad (25)
\end{aligned}$$

A MPO is exactly a vector in the form of MPS in $\mathfrak{H}$. Analogously, the entanglement in this vector is characterized by matrix rank [62]. Without treating the MPO perturbatively in β, this entanglement is explicitly determined by the lattice topology and the types of interactions. Nevertheless, the entanglement in the MPO is reduced in a simple yet systematic way in this method. It is called the entanglement perturbation theory for a quantum Hamiltonian. The benefit of entanglement reduction in MPO is immediate in that it reduces an eigenvalue problem of rank of $4^N P^2$, which dominates over the GEEs of rank of $2^N P^2$ in terms of computational burden, to that of rank of $(3N+1)P^2$. It is clear that the bottleneck of simulation of an $\infty \times N$ Heisenberg lattice becomes how to efficiently solve GEEs. When $N = 14$ and $P = 350$ (the parameters causing the most computational burden in this work), their rank is more than 2×10^9 . Solving such a large GEE is not feasible with any existing numerical tool. Thus, we integrate the Jacobi-Davidson method with MPS and MPO to solve the GEEs without explicitly forming them. The details are explained in Sec. II F.

D. Entanglement entropy and area law in Hilbert space

It is the entanglement in Hilbert space between an isolated quantum lattice set I and the surrounding environment E that is of special interest in the design of a many-body method that uses MPS since the area law [61] states that

$$s(I) \propto |\partial I| \qquad (26)$$

and

$$s(I) \leqslant 2\log_2(P), \qquad (27)$$

where $|\partial I|$ is the area of boundary ∂I and P is the MPS rank. The *von Neumann* entanglement entropy $s(I)$ is defined as

$$s(I) \equiv -\sum_i \rho_i \log_2 \rho_i. \qquad (28)$$

Now that the local Hilbert space $\mathcal{H}_\mathcal{I} \equiv \{|\phi_i\rangle\}$ is embedded in the complete Hilbert space $\mathcal{H}$ to write a system wave function $|\Psi\rangle$, the reduced density matrix is

$$\rho_{ij} = \mathrm{Tr}_E \langle\phi_i|\Psi\rangle\langle\Psi|\phi_j\rangle. \qquad (29)$$

In the case where $|\Psi\rangle$ is expressed as a MPS, the reduced density matrix is evaluated as shown in Eq. (59). See Sec. II G for details. After diagonalizing the reduced density matrix, the entanglement entropy can be readily computed using the diagonal density matrix elements.

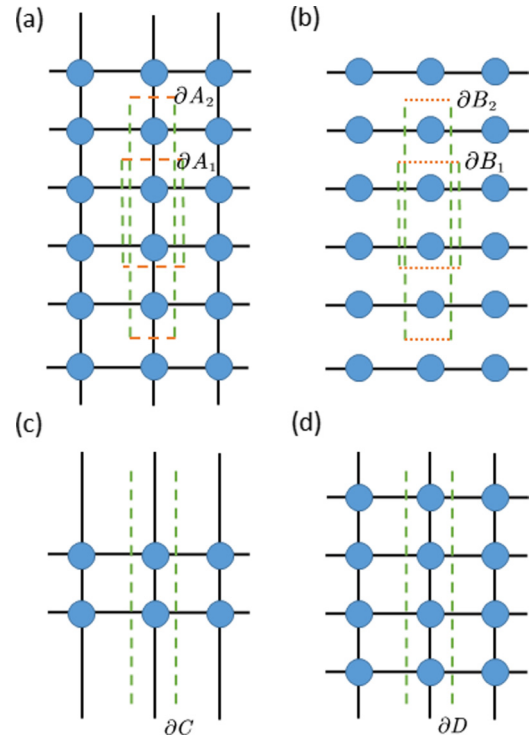

FIG. 5. Schematic of applicable and inapplicable scenarios of the area law. Applicable: (a) isolations embedded in a large 2D lattice whose sites (circles) interact along both dimensions (solid lines). The boundaries in dashed lines are enclosed; (b) the boundary of isolation embedded in a decoupled lattice shows no difference with or without the horizontal dotted lines to enclose them. Inapplicable: from (c) to (d), the width N of the ladder is increasing. They are described by two distinct Hamiltonians. For $N = \infty$ in both (a) and (d), the boundaries are topologically different. The former is single connected while the latter is disconnected.

Figure 5(a) shows the applicable scenario of the area law. An isolated partition increases from A_1 to A_2, embedded in a given large 2D quantum lattice whose sites (shown as circles) interact both horizontally and vertically (shown as solid lines). Note that the boundaries ∂A_1 and ∂A_2 are composed of both vertical and horizontal dashed lines. When the isolated partition is enlarged, its boundary increases nearly linearly. According to Eq. (27), the MPS rank P which is required to obtain a certain precision for the nearly linearly increasing entanglement entropy should almost exponentially increase. Since all the existing many-body methods such as DMRG, density matrix embedding theory (DMET) [66], and dynamic mean field theory (DMFT) [67] start from or focus on an isolated quantum lattice set surrounded by a large environment as shown in Fig. 5(a), they encounter the same

difficulty originating from the area law of entanglement entropy.

In our method of converting the N lattice sites in the rung into an effective site and then building a MPS on the effective chain, there are two major differences from the scenario shown in Fig. 5(a). First, two lattices of N_1 shown in Fig. 5(c) and N_2 in Fig. 5(d) actually have two different Hamiltonians. Second, imagining $N = \infty$ in both Figs. 5(a) and 5(d) such that their Hamiltonians are identical, their boundaries ∂A_∞ and ∂D_∞ are topologically different because the former is connected and the latter is disconnected. Therefore, the entanglement of isolations A in Fig. 5(a) and D in Fig. 5(d) is different. That is to say, the area law of entanglement entropy is not applicable in our method.

However, Figs. 7 and 8(c) in Sec. III confirm that the area law coincidentally applies when we solve the decoupled spin ladder [Fig. 5(b)] using our method. There are two reasons. First, Hamiltonian $H(n)$ of a decoupled spin ladder of $N = n$ now has the perfect extensivity property, i.e., $H(n) = nH(1)$ where $H(1)$ is the spin chain Hamiltonian. Second, there is no difference whether or not the boundary is enclosed by the dotted horizontal lines because there is no vertical interaction.

In fact, the entanglement entropy is crucially controlled by the density matrix of an effective site when our method is used to study a quantum ladder. Let us consider the following two ideal cases.

Case 1. The Hamiltonian is perfectly extensive, i.e., $H(n) = nH(1)$ with n being an integer. The decoupled ladder clearly qualifies for this category. In this case, the diagonalized density matrix $(\rho(nI))$ of the isolated partition nI is the direct product of $(\rho(I)) = \left(\begin{smallmatrix} x & 0 \\ 0 & y \end{smallmatrix}\right)$ for n times. Then, the diagonal element of $(\rho(nI))$ forms a set $\{x^k y^{n-k}; k = 0, \ldots, n\}$ with $\binom{n}{k}$-fold degeneracy. We have

$$\begin{aligned} s(nI) &= -\sum_{k=0}^{n} \binom{n}{k} x^{n-k} y^k \log_2(x^{n-k} y^k) \\ &= n\left[\sum_{k=0}^{n-1} \binom{n-1}{k} x^{n-1-k} y^k\right](-x \log_2 x - y \log_2 y) \\ &= n(x+y)^{n-1} s(I). \end{aligned} \tag{30}$$

Since $x + y = 1$ holds, we have

$$s(nI) = ns(I). \tag{31}$$

The area law evidently applies.

If x is equal to y, i.e., if the diagonalized density matrix is always equally weighted regardless of the size of nI, there is no dominant element. The MPS rank P that reveals the physical properties such as GS energy to a certain precision should be equal to what reveals the entanglement (i.e., the Fock vector configuration) in a wave function. Equation (27) determines that P strictly exponentially increases with N for a desired energy accuracy. Meanwhile, the diagonalized density matrix of a decoupled ladder of width N always has dominant elements because $x \neq y$ for a single chain. In turn, our result in Sec. III shows that the increase of P will be slower than an exponential function of N for smaller N's but will asymptotically tend to an exponential function 2^N for $N \to \infty$.

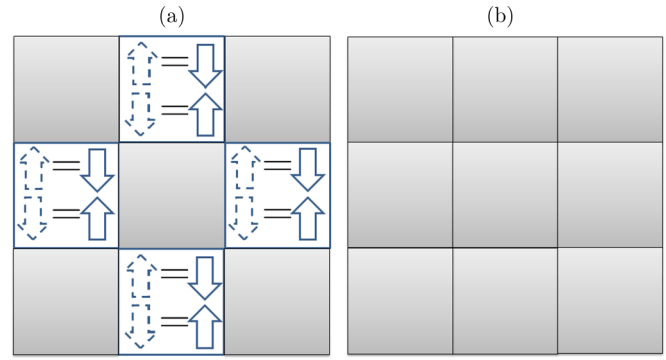

FIG. 6. (a) Owing to the antiferromagnetic nature, the tensors of MPO and MPS have a bipartite checkerboard symmetry in the original spin basis. (b) After applying the checkerboard transformation on any sublattice, for instance the blank lattice as shown, those tensors need not be distinguished anymore in the new spin basis.

Case 2. There are a limited number of dominant diagonal elements. We discuss an extreme example:

$$\rho_1 = 1 - 2^{-n}, \quad \sum_{i=2}^{\mathcal{R}(\mathcal{H}_{nI})} \rho_i = 2^{-n}. \tag{32}$$

Here, $\mathcal{R}(\mathcal{H}_{nI})$ is the Hilbert space rank of nI, and $\rho_{i=2,\ldots,\mathcal{R}(\mathcal{H}_{nI})}$ are equally weighted. In this case, it is easy to show that $s(nI) < ns(I)$ and that the entanglement entropy saturates when n is large. The area law does not apply.

In a realistic strongly coupled $\infty \times N$ spin lattice, our results in Secs. III and IV confirm that the area law of entanglement entropy does not apply and the density matrix of an effective site has few, not single, dominant diagonal elements whose number saturates with increasing N.

Letting an effective site have a large local space, our method takes the dominant basis vectors into account so as to simulate the physical quantities efficiently with a smaller MPS rank. Packing the entanglement contributed by the dominant basis vectors in a smaller MPS by coarse graining N quantum lattices in the rung is an implicit entanglement perturbation in the Hilbert space. It is also possible to truncate the local (i.e., at an effective site) Hilbert space by removing the diagonalized density matrix elements whose contributions are negligible. It amounts to a space reduction in MPS. We present the details in Sec. II G. For the moment, we discuss in the following two subsections other specific properties of the model in this study.

E. Implementation of checkerboard symmetry

So far, we have assumed a bipartite structure for both MPO and MPS according to the antiferromagnetic nature of the studied model. All the formulations can be straightforwardly extended for even more complicated structures. In an opposite limit, we specifically simplify both MPO and MPS to employ a single tensor Γ and ξ by a checkerboard transformation applied to a sublattice shown in Fig. 6(a) as

$$|\uparrow'\rangle \equiv |\downarrow\rangle, \quad |\downarrow'\rangle \equiv |\uparrow\rangle. \tag{33}$$

Assuming the second site within a bond is on the transformed sublattice, we rewrite H_{bond} as

$$H_{\text{bond}} = \vec{S}_i \cdot \vec{S}_j = S_i^z \cdot S_j^z + \tfrac{1}{2}(S_i^+ \cdot S_j^- + S_i^- \cdot S_j^+), \quad (34)$$

where S^+ and S^- are the operators to flip the spin up or down, respectively. They operate on the transformed site as

$$\begin{aligned} S^z|\uparrow'\rangle &= -\tfrac{1}{2}|\uparrow'\rangle; & S^z|\downarrow'\rangle &= \tfrac{1}{2}|\downarrow'\rangle \\ S^+|\uparrow'\rangle &= |\downarrow'\rangle; & S^+|\downarrow'\rangle &= 0 \\ S^-|\uparrow'\rangle &= 0; & S^-|\downarrow'\rangle &= |\uparrow'\rangle. \end{aligned} \quad (35)$$

Equation (35) is used to rewrite H_{bond} in the checkerboard-transformed basis as

$$H_{\text{bond}} = -S_i^z \cdot S_j^z + \tfrac{1}{2}(S_i^+ \cdot S_j'^+ + S_i^- \cdot S_j'^-), \quad (36)$$

where S'^+ (S'^-) has the same matrix representation of S^+ (S^-) but flips up (down) the newly defined down (up) spins in Eq. (33). After the transformation, we simplify the MPS to have just one tensor ξ in Eq. (7) and the MPO to have just one tensor Γ in Eq. (6). The other related formulation will be simplified accordingly, and we only present the simplified formulations when they are specifically needed in the remainder of the discussion in this paper. Note that an appropriate sign is needed when a physical quantity is being calculated with the solved wave function in the checkerboard-transformed basis. Also, note that compared with Eq. (24) before the checkerboard transformation, the GS energy per spin now becomes

$$\bar{\epsilon}_0 = -(N\beta)^{-1}\ln\lambda, \quad (37)$$

where λ is the largest eigenvalue of the only remaining GEE.

F. Integration of Jacobi-Davidson eigenvalue solver for GEE with MPO and MPS

We discuss how to obtain the largest eigenvalue and the corresponding eigenvector by iteratively solving a GEE given by

$$Xx = \lambda Y x, \quad (38)$$

where X and Y are $n \times n$ square matrices, x is an eigenvector, and λ is the corresponding eigenvalue. When only a few eigenvectors are needed (only the largest eigenvalue is needed in this study) and when n is very large, an iterative approach such as the Jacobi-Davidson method [65] is more desirable than the typical method of factorization. It starts with an initial $n \times m$ matrix W_0 whose columns are n-element vectors w_i, $i = 1, \ldots, m \ll n$. It is used to transform X and Y to those of rank of m as

$$\begin{aligned} Z_0 &\equiv W_0^T X W_0, \\ F_0 &\equiv W_0^T Y W_0. \end{aligned} \quad (39)$$

The following new GEE

$$Z_0 y^0 = \tau^0 F_0 y^0 \quad (40)$$

is much easier to solve for all its eigenvalues $\{\tau_i^0\}$ and the corresponding eigenvectors $\{y_i^0\}$. $\{\tau_i^0\}$ are ordered such that $\tau_1^0 > \tau_2^0 > \cdots$. Then, a new vector is constructed as

$$Q_0 = \left(XW_0 - \tau_1^0 Y W_0\right) y_1^0. \quad (41)$$

To accelerate convergence, the vector Q_0 is processed to obtain a new vector w_{m+1} as

$$w_{m+1}(i) = \frac{Q_0(i)}{\tau_1^0 Y(i,i) - X(i,i)}, \; i = 1, \ldots, n. \quad (42)$$

w_{m+1} is attached as a new column to W_0 forming an $n \times (m+1)$ matrix W_1. In this procedure, the Gram-Schmidt method is used to make w_{m+1} orthonormal to the existing column vectors. The approximated eigenvector corresponding to the largest eigenvalue is

$$x_0 = W_0 y_1^0. \quad (43)$$

The precision of this approximation is checked by whether Xx_0 and Yx_0 are parallel. If so, the iteration stops with the solution of the largest eigenvalue τ_1^0 and the corresponding eigenvector x_0. If not, we carry on the process with

$$\begin{aligned} Z_1 &\equiv W_1^T X W_1, \\ F_1 &\equiv W_1^T Y W_1 \end{aligned} \quad (44)$$

until Xx_j and Yx_j are parallel at the jth step. Satisfactory convergence is obtained after about 100 steps in this study even for GEE of rank of billions.

So far, we introduced the basic steps of the Jacobi-Davidson method for the GEE. The steps are merely formal because matrices X and Y in fact never appear in the explicit form as shown in Eqs. (39), (41), and (44). They even cannot be generated and stored when their rank is greater than 10^5, which turns out to be still much below the requirement to investigate the long-range spin-spin correlation in this study. As a workaround, we integrate the aforementioned Jacobi-David method with MPS and MPO, without explicitly forming the left and right matrices of GEE.

After the checkerboard transformation, we only need one MPO tensor Γ that is still formulated as in (5). Γ is extremely sparse. We only store its nonzero elements in $\{\Omega_j : |\Omega_j| > 0\}$ and the set $\{(r_j, s_j, \alpha_j, \gamma_j)\}$, each of whose elements is an array of the indices of the jth nonzero element $\Omega_j \equiv \Gamma_{r_j s_j, \alpha_j \gamma_j}$. Now, we simplify X and Y in Eq. (20) as

$$\begin{aligned} X_{\lfloor r,\alpha_1,\gamma_1\rfloor,\lfloor s,\alpha_3,\gamma_3\rfloor} &= v_{\alpha_1\alpha_2\alpha_3}\Gamma_{rs,\alpha_2\gamma_2}u_{\gamma_1\gamma_2\gamma_3}, \\ Y_{\lfloor r,\alpha_1,\gamma_1\rfloor,\lfloor s,\alpha_3,\gamma_3\rfloor} &= v'_{\alpha_1\alpha_3}\delta_{r,s}u'_{\gamma_1\gamma_3}. \end{aligned} \quad (45)$$

These are dense matrices. The notion of the effective site's label is no longer needed since the lattice is translationally symmetric after the checkerboard transformation.

Except for explicitly evaluating Eq. (45) for the diagonal element of X and Y that is needed in Eq. (42), the matrix-vector multiplication only in which X and Y explicitly participate in an operation [Eqs. (39), (41), and (44)] can be evaluated as

$$z_{\lfloor r,\alpha_1,\gamma_1\rfloor} = \sum_j v_{\alpha_1\alpha_j\alpha_3}\Gamma_{r_j s_j,\alpha_j\gamma_j}u_{\gamma_1\gamma_j\gamma_3}w_{\lfloor s_j,\alpha_3\gamma_3\rfloor}, \quad (46)$$

where r is dynamically updated by r_j during the summation over j. We further rewrite Eq. (46) as

$$z_{\lfloor r,\alpha_1,\gamma_1\rfloor} = \sum_j \Gamma_{r_j s_j,\alpha_j\gamma_j}(\pi^{\alpha_j}\cdot\varpi^{s_j}\cdot\rho^{\gamma_j})_{\alpha_1\gamma_1}. \quad (47)$$

In the parentheses, three new matrices are defined using the tensors appearing in (46) as

$$(\pi^k)_{ij} \equiv v_{ikj}; \quad (\varpi^k)_{ij} \equiv w_{\lfloor kij \rfloor}; \quad (\rho^k)_{ij} \equiv u_{jki}. \tag{48}$$

Note the difference in the right-hand side of the first and third equations in (48), which reflects the sandwich structure constructed by the MPS wave function, its conjugate, and the MPO. The newly defined matrices participate in a chain of multiplication to yield a resultant matrix that has two indices α_1 and γ_1 contracting with the MPO tensor Γ. Equation (47) is equivalent to update z with the resultant matrix L times, where L is the number of nonzero elements of Γ and these elements are the updating coefficients.

The transformation from expression of matrix-vector multiplication in Eq. (46) to that in (47) is crucial because the summations are broken into a successive matrix product of matrices, which reduces the computational cost by a few orders in the MPS rank P. Again, the mathematical idea of MPS to associate many loops of index summation by a successive matrix product helps reduce the computational burden when solving a GEE without even explicitly forming it.

Meanwhile, the SVDs in Eq. (15) are simplified after the checkerboard transformation as

$$\begin{aligned} A &= u\Lambda v, \\ C &= u'\Delta v', \end{aligned} \tag{49}$$

where

$$\begin{aligned} A_{\alpha\equiv\lfloor\alpha_1\alpha_2\alpha_3\rfloor,\gamma\equiv\lfloor\gamma_1\gamma_2\gamma_3\rfloor} &\equiv \xi_{r,\alpha_1\gamma_1}\Gamma_{rs,\alpha_2\gamma_2}\xi_{s,\alpha_3\gamma_3}, \\ C_{\alpha\equiv\lfloor\alpha_1\alpha_3\rfloor,\gamma\equiv\lfloor\gamma_1\gamma_3\rfloor} &\equiv \xi_{r,\alpha_1\gamma_1}\xi_{r,\alpha_3\gamma_3} \end{aligned} \tag{50}$$

have the rank of $T = (3N+1)P^2$ and $O = P^2$, respectively. Both of them will be very large in some cases. For instance, the largest T value encountered in this study is 1.0×10^8 when $P = 2000$ for $N = 8$. It is not accessible by ordinary SVD solvers. In this study, SVDs are solved by the power method without forming A and C. The matrix-vector multiplication is transformed into a successive matrix product similar to Eq. (47).

The composite matrices A, B defined in Eq. (9) have rank $(3N+1)P^2$; C and D defined in Eq. (11) have rank P^2. The composite-matrix-vector multiplication is the time-controlling factor in the Davidson method. It is decomposed to a chain of lower-ranked matrix-vector products after decomposing the composite matrix as in Eq. (47). The lower rank is P. Thus, the time consumption in iqEPT is bilinear with both $P^{2.5}$ (if using a Lapack routine) and 2^N (which determines the number of nonzero elements in Γ). In the largest simulation scale of this work, it took 2×10^4 s to solve the GEE in a series of iterations for $N = 10$ and $P = 1400$, using 6 Dual-Intel-Xeon nodes each of which has 20 cores and 256 GB memory installed. It took 50 iterations to obtain the converged data for that set of N and P.

G. Space reduction in matrix product state

The use of density matrix is crucial in simulating quantum lattice models in that it guides reduction of Hilbert space (subspace) which exponentially increases with respect to the system (subsystem) size. Given a bipartite structure A and E of a system, the system wave function $|\Psi\rangle$ is an entangled quantity composed of basis vectors from subspaces $\{|\phi_i\rangle\}$ for A and $\{|\psi_i\rangle\}$ for E,

$$|\Psi\rangle = \sum_{i,j} X_{ij}|\phi_i\rangle|\psi_j\rangle, \tag{51}$$

where X is a tensor entangling A and E. The density operator for a subspace, say $\{|\phi_i\rangle\}$, is defined as $\hat{\rho} \equiv \mathrm{Tr}_E|\Psi\rangle\langle\Psi|$, where Tr_E means that the degree of freedom in subsystem E is traced out. Its matrix representation is

$$(\rho_{ij}) \equiv \langle\phi_i|\hat{\rho}|\phi_j\rangle = X_{ik}X^*_{jk}. \tag{52}$$

Note that normalization of $|\Psi\rangle$ implies $\mathrm{tr}\rho = 1$.

The system wave function can be reconstructed as $|\Psi'\rangle$ using a reduced space $\{|\theta_i\rangle\}$ consisted of M basis vectors for A along with the unaltered space $\{|\psi_i\rangle\}$ for E. The density matrix built in $\{|\phi_i\rangle\}$ is used to make the residual vector $|R\rangle \equiv |\Psi\rangle - |\Psi'\rangle$ have a minimum norm [41,42,62]. Explicitly, the density matrix is diagonalized and only M eigenvectors $\{v_i; i = 1, \ldots, M\}$ need to be retained. They correspond to the most significant M diagonal elements $\{\eta_i\}$. New basis vectors are constructed as

$$|\theta_i\rangle = v_i(k)|\phi_k\rangle, \tag{53}$$

where $v_i(k)$ is the kth element of the eigenvector v_i. And, $|\Psi'\rangle$ is constructed as

$$|\Psi'\rangle = Y_{ij}|\theta_i\rangle|\psi_j\rangle \tag{54}$$

with

$$Y_{ij} = v_i(k)X_{kj}. \tag{55}$$

If the formal reduction is unitary (zero reduction), substituting Eqs. (53) and (55) into (54) restores the wave function in (51). When the truncation of space of A takes place (i.e., when the eigenvector matrix kept is rectangular, hence no longer unitary), we have

$$|\Psi'\rangle = X_{kj}v_i(k)v_i(l)|\phi_l\rangle|\psi_j\rangle = |\Psi\rangle - |R\rangle \tag{56}$$

with

$$|R\rangle = X_{kj}\Delta_{kl}|\phi_l\rangle|\psi_j\rangle. \tag{57}$$

Here, $\Delta_{ij} = \sum_{k=M+1}^{n} v_i(k)v_j(k)$. It is straightforward to show $|||R\rangle||^2 = \sum_{i=M+1}^{n}\eta_i$.

Following the line of local space reduction, DMRG uses the density matrix to keep a fixed number of transformed basis vectors for an enlarged part of the system. DMET provides an alternative to DMFT, using the density matrix to improve the impurity state of a fragment embedded in the background. We implement the density matrix in a different way where it is used to reduce spaces in MPS. Dividing a quantum lattice into L blocks each of which contains N physical sites, a MPS is built as follows:

$$|\Psi\rangle = \sum_{\ldots r^i \ldots r^L} \mathrm{tr}\big(\ldots \xi^{i-1}_{r^{i-1}} \cdot \xi^{i}_{r^i} \ldots\big) \ldots \big|\phi^{i-1}_{r^{i-1}}\big\rangle\big|\phi^{i}_{r^i}\big\rangle \ldots, \tag{58}$$

where each MPS tensor ξ^i is associated with a block, say, the ith block. Different from Eq. (7), the MPS in Eq. (58) has a

more general form. Its tensor does not necessarily have a unit-cell structure and the space index r^i runs from 1 to $Q \equiv R^N$ meaning that each of the N physical sites in a block has a general space rank R.

The computational burden of variational optimization for each MPS tensor is determined by both bonding rank P and space rank Q. One needs a tractable strategy to balance between choices of P and Q. Choosing blocks that contain more physical sites has the following benefits. First, there are fewer tensors to solve. Second, it uses smaller P to achieve the same precision. In the extreme case when a block contains the whole system, one only needs a MPS tensor of rank 1 to precisely represent the system wave function. However, as Q increases exponentially with N to exclude the possibility of building MPS on a block containing the whole system, one still needs to solve multiple MPS tensors, while the same computational resource only allows smaller P when N is larger.

We propose a scheme to overcome this difficulty when building MPS on a blocked quantum lattice. A MPS ranked P_1 in the original spaces $|\Psi\rangle_{\perp P=P_1}$ is used to construct density matrix for each block, say the ith block, as

$$\rho^i_{ab} = \mathrm{tr}\Big[\ldots\big(\xi^{i-1}_{r^{i-1},\alpha_1\gamma_1}\xi^{i-1}_{r^{i-1},\alpha_2\gamma_2}\big)\big(\xi^{i}_{a,\gamma_1\eta_1}\xi^{i}_{b,\gamma_2\eta_2}\big) \times \big(\xi^{i+1}_{r^{i+1},\eta_1\theta_1}\xi^{i+1}_{r^{i+1},\eta_2\theta_2}\big)\ldots\Big]. \tag{59}$$

In $\xi^i_{a,\gamma_1\eta_1}$, a denotes the space index and the bond indices γ_1 and η_1 are explicitly shown here. Note that the density matrix element in Eq. (59) should be adjusted according to the MPS normalization. Density matrices will be constructed for all L tensors (blocks) and are diagonalized simultaneously. For each block, only eigenvectors corresponding to the largest M diagonal elements are used to transform the space $\{|\phi^i_j\rangle\}$ to the smaller one $\{|\theta^i_j\rangle\}$ according to Eq. (53), where the superscript refers to the block's label.

The MPO tensor is correspondingly transformed as

$$\Gamma_{r's',mn} = v_{r'}(s)\Gamma_{rs,mn}v_{r'}(r). \tag{60}$$

Notice that only the space index is changed in Eq. (60). Also note that MPS in the reduced space set $\{H^{i,\prime} \equiv \{\theta^i_j\}\}$ for $P \leqslant P_1$, $|\Psi'\rangle_{\perp P\leqslant P_1}$, can be reconstructed from the existing MPS $|\Psi\rangle_{\perp P\leqslant P_1}$ as

$$|\Psi'\rangle = \sum_{\ldots s^i\ldots s^L} \mathrm{tr}\big(\ldots\kappa^{i-1}_{s^{i-1}}\cdot\kappa^{i}_{s^i}\ldots\big)\ldots\big|\theta^{i-1}_{s^{i-1}}\big\rangle\big|\theta^{i}_{s^i}\big\rangle\ldots \tag{61}$$

with

$$\kappa^i_a = v_a(b)\xi^i_b. \tag{62}$$

$|\Psi'\rangle_{\perp P>P_1}$ is then variationally determined. Alternatively, the MPS in reduced spaces can be variationally determined for all the ranges of P. The variational solution is described in Sec. II B. In both ways, $\{H^{i,\prime}\}$ has a smaller rank $Q' < Q$ and the same computational resource now allows larger P, yielding better accuracy in turn.

For the spin ladder studied in this work, we showed that the linking complexity between the building units of MPO is reduced to a linear dependence on N and the large-rank GEE is efficiently handled by integrating the Jacobi-Davidson method with MPS and MPO. The only remaining factor that gains exponential complexity with increasing lattice width is the space rank 2^N of an effective site. This rank has been crucial in handling even larger lattices or different complex scenarios by iqEPT. This exponential complexity is now systematically overcome by the space reduction in MPS.

Meanwhile, the density matrix can be used to reveal the system properties since it determines which kind of basis vector contributes the most in the GS wave function. To this end, we define the following quantity to reveal the spontaneous spin-rotational symmetry breaking:

$$\bar{S^z}_j \equiv \big\langle\theta^i_j\big|\sum_{k=1}^{N}(-1)^k S^z_{(i,k)}\big|\theta^i_j\big\rangle. \tag{63}$$

Here, $|\theta^i_j\rangle$ is the jth new basis vector in the space (only unitarily transformed, not necessarily reduced) of the ith effective site. (i,k) is the 2D coordinate of a physical site. For a wave function having the broken symmetry, one spin configuration is expected to have a larger amplitude than its upside-down counterpart in GS. It leads to nonzero values of $\bar{S^z}_j$ with the same sign for those $j's$ with non-negligible diagonal density matrix elements. In contrast, this quantity is zero when there is no spin-rotational symmetry breaking.

H. Spin-spin correlation and local magnetization

The spin-spin correlation is defined as $C_r \equiv \langle S^z_{(i,j)}S^z_{(i+r,j)}\rangle$ where the operators are separated by r sites along LD of an $\infty \times N$ lattice. Without loss of generality, we set $j = 1$. After converting the lattice into a chain of effective lattice sites, the operators are redefined as

$$S^z_{i,\mathrm{eff}} \equiv S^z_{(i,1)}\otimes I_{(i,2)}\otimes\cdots\otimes I_{(i,N)}, \tag{64}$$

where $I_{(i,m)}$ is an identity operator operating on (i,m)th physical lattice site.

It is straightforward to construct a tensor Θ for $S^z_{i,\mathrm{eff}}$. After implementing the checkerboard transformation, the same tensor also applies to $S^z_{i+r,\mathrm{eff}}$. Therefore, the correlation function is written as

$$C_r = \frac{\mathrm{tr}\Big[\ldots\big(\xi_{s^i,\alpha_i\alpha_{i+1}}\Theta_{s^ir^i}\xi_{r^i,\gamma_i\gamma_{i+1}}\big)\cdot\big(\xi_{s^{i+1},\alpha_{i+1}\alpha_{i+2}}\xi_{s^{i+1},\gamma_{i+1}\gamma_{i+2}}\big)\ldots\big(\xi_{s^{i+r},\alpha_{i+r}\alpha_{i+r+1}}\Theta_{s^{i+r}r^{i+r}}\xi_{r^{i+r},\gamma_{i+r}\gamma_{i+r+1}}\big)\ldots\Big]}{\mathrm{tr}\Big[\ldots\big(\xi_{s^i,\alpha_i\alpha_{i+1}}\xi_{s^i,\gamma_i\gamma_{i+1}}\big)\cdot\big(\xi_{s^{i+1},\alpha_{i+1}\alpha_{i+2}}\xi_{s^{i+1},\gamma_{i+1}\gamma_{i+2}}\big)\ldots\Big]}. \tag{65}$$

We convert the quantities in the first and second parentheses in the numerator of Eq. (65) to matrices G and B as we did in Eq. (9) in Sec. II B. Equation (65) becomes

$$C_r = \lim_{M\to\infty}\frac{\mathrm{tr}(G\cdot B^r\cdot G\cdot B^{M-r-2})}{\mathrm{tr}(B^M)}. \tag{66}$$

Since Eq. (66) only yields positive values, a proper sign should be given to $C(r)$ according to even or odd r, to reflect the checkerboard transformation. We do SVD on B as $B = \mu\varrho\nu$. The singular values $\{\varrho_i\}$ are sorted in descending absolute magnitude. Equation (66) leads to

$$C_r = \frac{\mathrm{tr}\left(\nu_1^T \cdot G \cdot B^r \cdot G \cdot \mu_1\right)}{\varrho_1^{r+2}}. \tag{67}$$

When $r \to \infty$, we have

$$C_\infty = \frac{F_1^2}{\varrho_1^2} \tag{68}$$

with

$$F_1 \equiv \nu_1^T \cdot G \cdot \mu_1. \tag{69}$$

The numerator may be zero or nonzero, giving disorder including quasi-long-range order (QLRO) or order of the lattice. Moreover, it is straightforward that the local magnetization is

$$\bar{M} \equiv \langle S^z \rangle = \lim_{M\to\infty} \frac{\mathrm{tr}(G \cdot B^{M-1})}{\mathrm{tr}(B^M)} = \frac{F_1}{\varrho_1}. \tag{70}$$

Thus, we arrive at a theorem that the spin-spin correlations after infinite spin-spin separation is square of the local magnetization,

$$C_\infty = \bar{M}^2. \tag{71}$$

This theorem is a useful supplement to the commonly used definitions relating spin-spin correlations to staggered magnetization [6] though they are not universally agreed upon [68].

A new quantity

$$\tau_r \equiv \ln(\ln C_r - \ln C_{r+1}) \tag{72}$$

is shown in Sec. IV to be useful. Although only the largest eigenvalue of B determines the asymptotic C_∞, the first eigenvalue $\varrho_{\bar{k}}$ that has significant nonvanishing

$$F_{\bar{k}} \equiv \nu_1^T \cdot G \cdot \mu_{\bar{k}} = \nu_{\bar{k}}^T \cdot G \cdot \mu_1 \tag{73}$$

is also important in determining how C_r approaches C_∞ asymptotically. Given

$$C_r \approx \frac{F_1^2}{\varrho_1^2} + \frac{F_{\bar{k}}^2}{\varrho_1^2}\left(\frac{\varrho_{\bar{k}}}{\varrho_1}\right)^{r-1}, \tag{74}$$

there are different scenarios of τ_r versus r after F_1 is converged with P.

Case 1. $F_1 \neq 0$. The lattice is ordered. We have

$$\tau_r \approx (r-1)(\ln\varrho_{\bar{k}} - \ln\varrho_1) + f \tag{75}$$

with

$$f \equiv 2(\ln F_{\bar{k}} - \ln F_1) + \ln(1 - \varrho_{\bar{k}}/\varrho_1). \tag{76}$$

Equation (75) reads that τ_r is linear with r. The slope of τ_r versus r is a nonzero constant $p_0 \equiv \ln\varrho_{\bar{k}} - \ln\varrho_1$. Then, $\ln C_r$, hence, C_r becomes constant for large r.

Case 2.1. $F_1 = 0$ and $\varrho_{\bar{k}}$ is significantly smaller than ϱ_1. Equation (74) reads as

$$C_r \approx \frac{F_{\bar{k}}^2}{\varrho_1^2}\left(\frac{\varrho_{\bar{k}}}{\varrho_1}\right)^{r-1} \tag{77}$$

and

$$\tau_r \approx \ln(\ln\varrho_1 - \ln\varrho_{\bar{k}}). \tag{78}$$

τ_r is a constant for large r. C_r decays exponentially with r. The lattice is disordered and gapped.

Case 2.2. $F_1 = 0$ and the first few largest eigenvalues are almost degenerate with ϱ_1 while having less significant F_j. They give small but slowly decaying contribution to the correlation. Eigenvalues which have significant F_j's are, however, definitely smaller than ϱ_1. They give to the correlation contribution that is large for small r but decays exponentially. All summed up, the resultant correlation function shows a power-law decay in a large range of r. τ_r is linear with $\ln(r)$ instead of r. The lattice is QLRO. See Appendix A for an example with the spin chain.

III. BENCHMARK

In order to check the correctness of our algorithm, we benchmark the method on decoupled spin-$\frac{1}{2}$ ladders for various width N's. Regardless of N, the ground-state energy per site ϵ_0 should be equal to the exact value $-0.443\,147$ by Bethe ansatz [3] of a single spin chain. Previously, the results for $N = 1$ along a similar line of reasoning were reported [36] to agree with the exact results. There was no need to utilize the entanglement reduction in MPO described in Sec. II C and the algorithm extensions presented in this work were not applied. For $N = 2$, our extended algorithm reproduced the exact energy at $P = 2000$, proving its correctness.

Figure 7(a) shows a linear log-log relationship between the error of iqEPT data, relative to the exact value, and the MPS rank P. Figure 7(b) further shows that the ratio of P_N (for N) to P_{N-1} (for $N-1$) approaches 2 when $1/N \to 0$. This indicates that P will asymptotically increase as an exponential function 2^N when $N \to \infty$. This increase is very rapid. For example, the MPS rank needed to obtain an energy accuracy of 99.99% is about 6×10^5 for $N = 6$. It is clear that treating a decoupled spin ladder by iqEPT is inefficient.

We compute the entanglement entropy according to Eq. (28) after diagonalizing the density matrix of a rung obtained in Eq. (59). Figure 8(a) shows that it has a linear dependence on $P^{-1/3}$. It can be used to make reliable extrapolations used in Fig. 8(c). The linear dependence of the entanglement entropy versus N, shown as open circles, confirms our prediction in Sec. II D that the area law of entanglement entropy coincidentally applies to decoupled ladders in our method. Note that the convergence of entropy is continuous in Fig. 8(a) for the gapless decoupled ladders. In what follows, however, the scenario changes drastically for an isotropically coupled spin ladder with either PBC or open boundary condition (OBC) imposed along the rungs. First is the ladder with OBC along the rungs for N up to 6, to directly compare with the existing methods in the literature.

The solid circles in Fig. 8(c) show that the area law does not apply to the coupled ladder (see Sec. II D for explanation). Also, the sudden convergence of entanglement entropy in Fig. 8(b) shows that the coupled ladder with OBC along the rungs is gapped [61] for $N = 2$, 4, and 6. However, the gap does not exponentially decay with increasing N because the

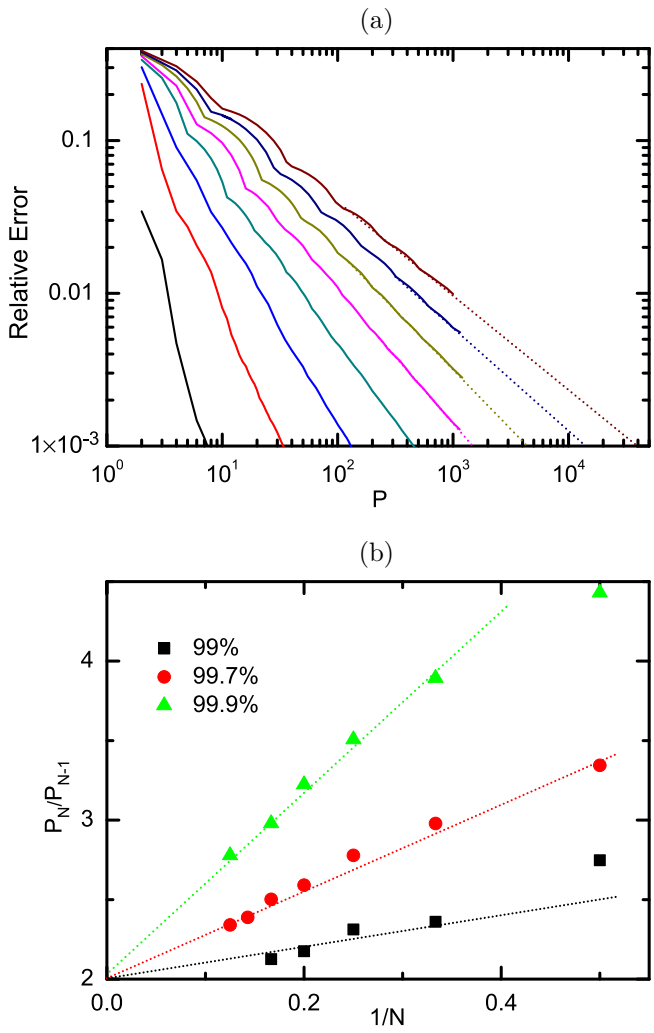

FIG. 7. (a) Relative error versus MPS rank P for decoupled ladders of $N = 1, 2, 3, 4, 5, 6, 7$, and 8, ordered from left to right. (b) Ratio of P_N and P_{N-1} with respect to $\frac{1}{N}$. At both P_N and P_{N-1} the same accuracy is obtained. The comparison is made for accuracies 99.9%, 99.7%, and 99% from top to bottom.

entanglement entropy will otherwise be linear [61,70,71] with N. This observation does not yet violate NLSM's prediction on the exponential decay of the gap because this prediction only applies to the coupled ladder with PBC in the rung. To confirm this, the entanglement entropy in the target model (the coupled ladder with PBC in the rung) is computed. Figure 13(c) partially confirms the prediction for $N = 2$, 4, and 6, as the entropy segment within this interval of N is indeed linear. Nevertheless, the saturation starting from $N = 8$ suggests that NLSM's prediction does not apply to larger N's. See Sec. IV for details. For the moment, we continue to use the model with OBC to compare with the existing methods.

Since there is no exact result to calculate the relative error directly, we extrapolate the asymptotic energy $\bar{\epsilon} \equiv \epsilon_{P\to\infty}$ to obtain the relative error. Assuming a power relationship between the relative error and P in iqEPT for isotropically coupled ladders, the parametrized sum of squared residuals is

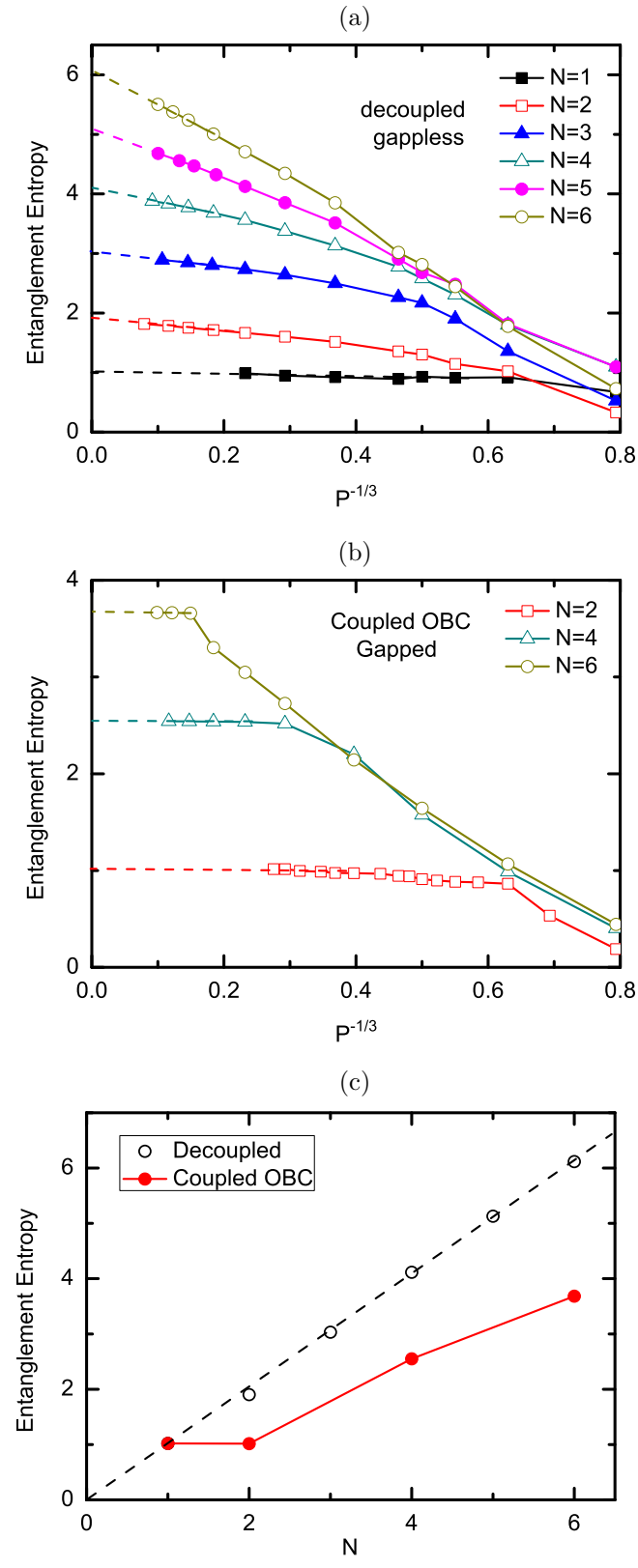

FIG. 8. Entanglement entropy of a rung versus $P^{-1/3}$ for (a) decoupled ladders and (b) coupled ladders with OBC in the rung. (c) Entanglement entropy versus N. Open and solid circles represent coupled and decoupled ladders, respectively.

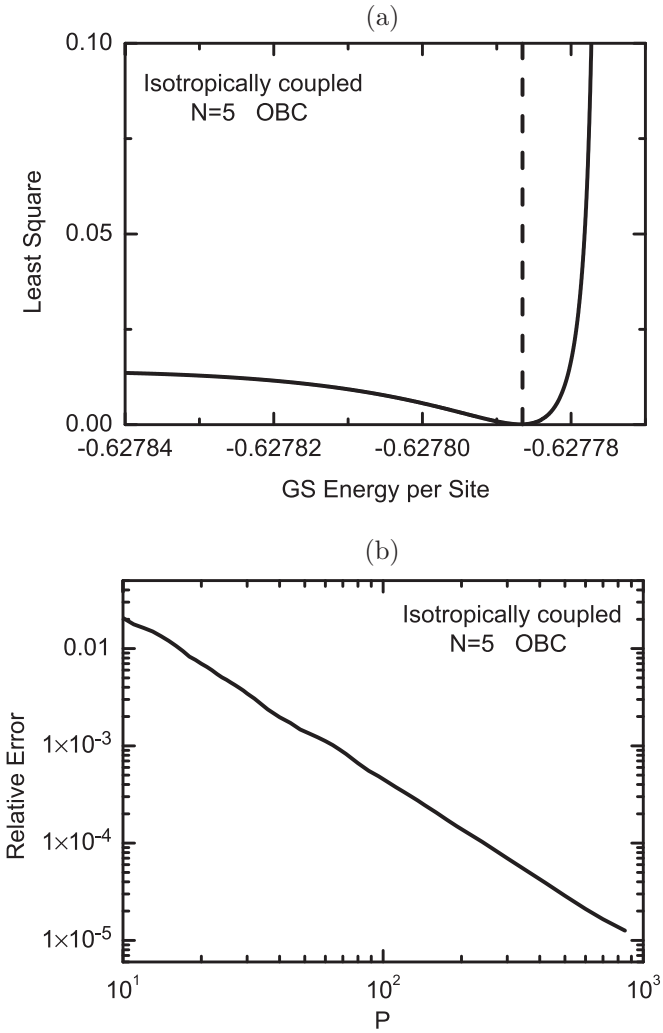

FIG. 9. (a) Sum of squared residuals versus GS energy per site and (b) log-log view of relative error versus MPS rank P for an isotropically coupled ladder of $N = 5$ with OBC along the rungs. The minimum of curve in (a) gives the extrapolation at $P \to \infty$ for GS energy per site needed to calculate the relative error in (b).

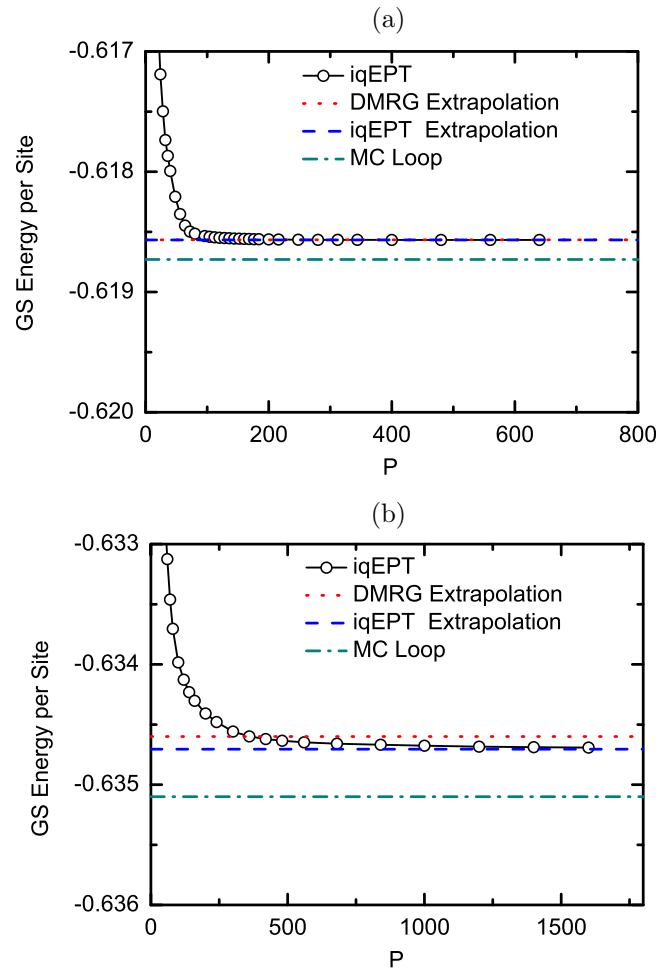

FIG. 10. Comparison of GS energy per site for spin ladders of (a) $N = 4$ and (b) $N = 6$ both in the energy scale of 0.003, by iqEPT, DMRG, and the MC loop algorithm. The short dotted line indicates the DMRG extrapolation. Circled iqEPT results converge to its dashed extrapolation.

defined as

$$l(\bar{\epsilon}) \equiv \sum_i \left(b_1 \log P_i + b_2 - \log \frac{\bar{\epsilon} - \epsilon_{P_i}}{\bar{\epsilon}} \right)^2 \tag{79}$$

with

$$b_1 = \frac{m \sum_i \log P_i \log \frac{\bar{\epsilon} - \epsilon_{P_i}}{\bar{\epsilon}} - \sum_i \log P_i \sum_i \log \frac{\bar{\epsilon} - \epsilon_{P_i}}{\bar{\epsilon}}}{m \sum_i (\log P_i)^2 - \left(\sum_i \log P_i \right)^2},$$
$$b_2 = \frac{1}{m} \left(\sum_i \log \frac{\bar{\epsilon} - \epsilon_{P_i}}{\bar{\epsilon}} - b_1 \sum_i \log P_i \right). \tag{80}$$

TABLE I. Comparison of GS energy per site among iqEPT, DMRG, and the MC loop algorithm for spin ladders with open boundary condition imposed along the rungs.

	iqEPT				DMRG [30]	
N	P'	$\epsilon_{P'}$	Extrapolation	Δ	Extrapolation	MC loop [69]
2	40	−0.578043	−0.578043		−0.578043	−0.57802
3	500	−0.600538	−0.600538		−0.600537	−0.60063
4	640	−0.618567	−0.618567		−0.618566	−0.61873
5	1200	−0.627781	−0.627787	9.6×10^{-6}	−0.62776	−0.62784
6	1600	−0.634681	−0.634690	1.4×10^{-5}	−0.6346	−0.635(1)

TABLE II. The simulated GS energy per site $\epsilon_{P'}$ at the largest MPS rank tried P', the extrapolated energy $\bar{\epsilon}$, and the relative error Δ for various N's of an $\infty \times N$ lattice with periodic BC imposed in both directions. The extrapolation for $N = 14$ is replaced by the interpolation in Fig. 11(c).

N	P'	$\epsilon_{P'}$	$\bar{\epsilon}$	Δ
2	32	−0.85935	−0.85935	
4	266	−0.68328	−0.68329	1.5×10^{-5}
6	560	−0.67277	−0.67279	3.0×10^{-5}
8	2000	−0.67074	−0.67078	6.0×10^{-5}
10	1400	−0.66996	−0.67017	3.1×10^{-4}
12	560	−0.66871	−0.67001	1.9×10^{-3}
14	350	−0.66636	−0.66993	5.3×10^{-3}

Minimizing Eq. (79) gives the optimal extrapolation $\bar{\epsilon}$. Figure 9(a) shows an example of such extrapolation for $N = 5$. Figure 9(b) confirms the assumed power relationship, making the extrapolation self-consistent.

Extrapolations are made for all ladders in comparison. Figure 10 shows that the GS energies for $N = 4$ and 6 have converged in the scale shown. Table I compares results by iqEPT, DMRG [30], and the MC loop algorithm [69]. Data given by DMRG in [30] are not the raw data but their extrapolation after two loops of scaling which vary both the finite ladder length and the number of kept diagonal elements in density matrix. Both Fig. 10 and Table I show that the discrepancy between iqEPT results (including extrapolation) and DMRG extrapolation rapidly increases when N increases from 4 to 6. Explicitly, it is 1.62×10^{-6} (1.62×10^{-6}) for $N = 4$ and 1.28×10^{-4} (1.42×10^{-4}) for $N = 6$, increasing by two orders in magnitude. For larger N, the discrepancy is expected to be progressively larger. As the next subsection will show, for the ladder of interest which has PBC imposed in both directions, the relative error of iqEPT result at $P = 2000$ for $N = 8$ is about 7.5×10^{-5}. For $N = 12$, it is about 10^{-3}. See Table II for details. It is obvious that the relative error in iqEPT scales much more slowly with respect to N than that in DMRG for a spin ladder.

One last interesting observation is that the ladders with OBC along the rungs are computationally more demanding in iqEPT. For instance, to obtain the same relative error 3.0×10^{-5} for $N = 6$, $P = 900$ is required for OBC while $P = 560$ for PBC. In contrast, DMRG favors OBC [62]. This difference has twofold meaning. First, the entanglement entropy of a rung in the ladder with OBC [solid circles in Fig. 13(c)] is greater than that with PBC [Fig. 13(b)] for each N in comparison. It determines that OBC along the rungs is necessarily more challenging to simulate. Second, DMRG's difficulty with PBC is caused by the winding MPS form [61] [Fig. 2(b)].

IV. RESULTS

A. Ground-state energy

Our target model is the isotropically coupled ladder of even N's, with PBC imposed in both directions. One of our main results is the GS energy per site for N up to 14, shown in Fig. 11. In Fig. 11(a), the varying of energy with respect to the MPS rank P is hardly noticeable for a large-P value in the energy scale of 0.1 shown for N up to 12. Recall that Fig. 7 shows a power relationship between the relative error and P and shows negative linear coefficients b_1 defined in Eq. (80). Therefore, the straight lines of energy versus $1/P$ should give reliable extrapolations when $1/P \to 0$, which is a simpler alternative to the extrapolating process in Eq. (79). Figure 11(b) shows energy versus $1/P$ in the scale of 0.01 for $N = 6$, 8, 10, and 12 from bottom to top, with the scale of 0.001 for $N = 4$ in the inset. Indeed, the straight lines steadily approach the extrapolations. Table II lists the largest MPS rank P' used for each N, the simulated GS energy per site $\epsilon_{P'}$, the extrapolated energy $\bar{\epsilon}$, and the relative error Δ. Note that the kept digits of $-0.859\,345\,7(1)$ with $P \geqslant 16$ for $N = 2$ is much more than other N's. We plot the extrapolated energies for each N versus N^{-4} in Fig. 11(c). Only data for $N = 6$, 8, 10, and 12 are shown due to the very fast decay of N^{-4}. They quickly approach the thermodynamic limit value of $-0.669\,84$ with an uncertainty of 9.6×10^{-6}. Our value agrees well with the accepted values such as -0.6696 ± 0.0003 by series expansions [72] and $-0.6693(1)$ by the cluster algorithm [73]. It can be compared with the DMRG result of -0.6768 [30]. It is worth mentioning that the finite-size effect fades away in our work by one order of $1/N$ faster than when approaching from $N \times N$ lattice. The energy for an $\infty \times N$ ($N = 12$) lattice has a 2.5×10^{-4} difference relative to the thermodynamic limit value, as close as that for a 22×22 lattice (interpolation from Fig. 5 of [6]).

Meanwhile, the most intriguing information from the energy observation is the plot in Fig. 12(a). It shows the ratio of the MPS rank for a given accuracy, say, 1.9×10^{-3} for N to that for $N - 2$, with respect to $1/N$. Figure 12(b) explains how to get each P_N. In Fig. 12(a), the dashed guiding line shows the tendency of $P_N/P_{N-2} = 1$ with $1/N \to 0$. This implies that the increase of entanglement in a MPS wave function built on an effective 1D lattice, whose site is converted from the N sites in the rung of an $\infty \times N$ lattice, will slow down with N and possibly will be saturated for larger N.

The mechanism of this saturation of P with N is accounted for by the saturating entanglement entropy of an effective site, shown in Fig. 13(b). It is now clear that, treating an $\infty \times N$ lattice as if in 1D does bypass the area law of entanglement entropy for the strongly correlated 2D quantum system if only larger N can be reached. Figure 13(a) shows that the computed entanglement entropy has a linear dependence on $P^{-1/3}$. For the ladders of $N = 2$, 4, and 6, it does suddenly converge [61] when P reaches a threshold, forming plateaus shown in the inset. Recall that the definitely gapless decoupled ladder shows continuous convergence of entanglement entropy with respect to the MPS rank in Fig. 8(a). Now that the ladders of $N = 8$, 10, and 12 show no plateau either, it is necessary to check whether the sudden convergence of a gapped ladder is not reached yet or the ladder is gapless. These two possibilities shall be explored with more physical quantities. At the moment, however, an immediate assertion can be made that, starting from $N = 8$, the lattice is out of the applicable regime of NLSM's prediction that the ladder has a gap which exponentially decays with increasing width. Otherwise, the entanglement entropy would be linear in the full range of N.

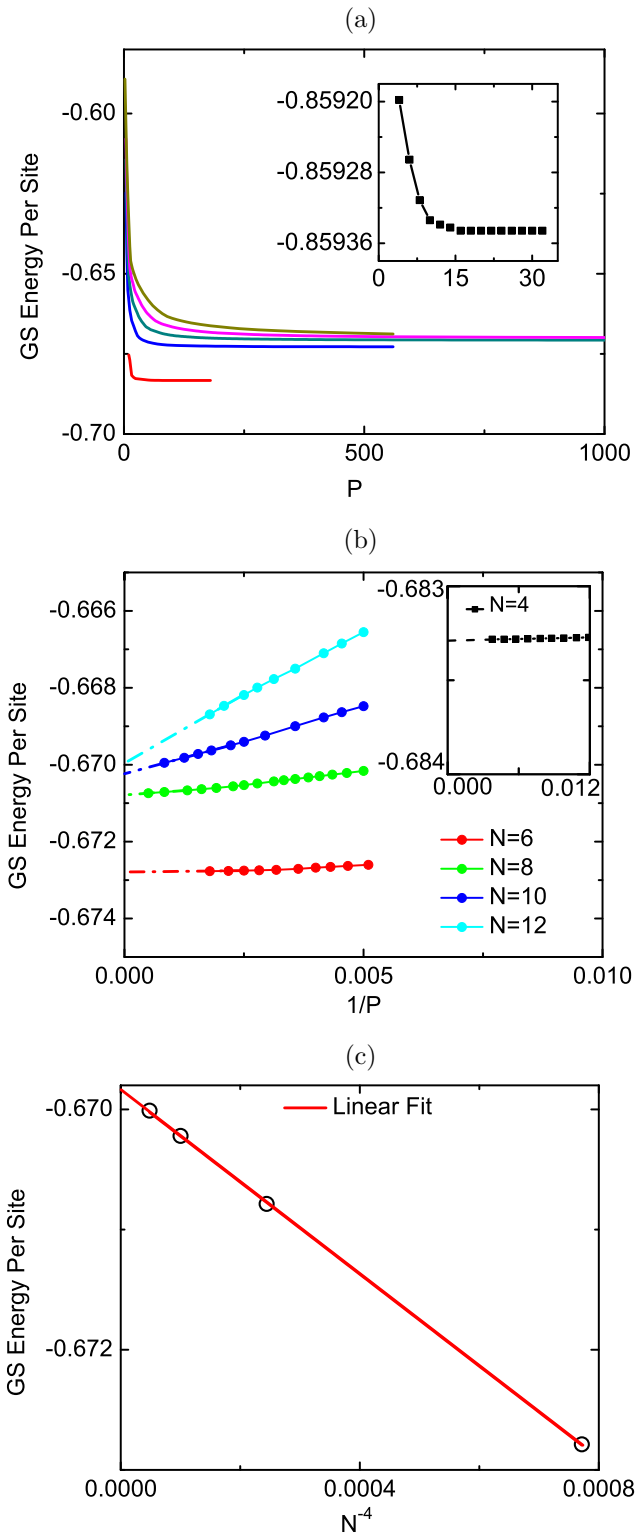

FIG. 11. (a) The convergence of GS energy per site with respect to the MPS rank P, for $N = 4, 6, 8, 10$, and 12 from bottom to top. The inset is for $N = 2$ in a distinct energy scale. (b) The convergence of energy with respect to $1/P$. The inset is for $N = 4$ in a distinct energy scale. They give extrapolations used in (c). (c) The GS energy per site approaches the thermodynamic value as a fourth-order function of $\frac{1}{N} \to 0$, one order faster than the approach from $N \times N$ lattices. Only data for $N = 6, 8, 10$, and 12 are shown due to the very fast decay of N^{-4}.

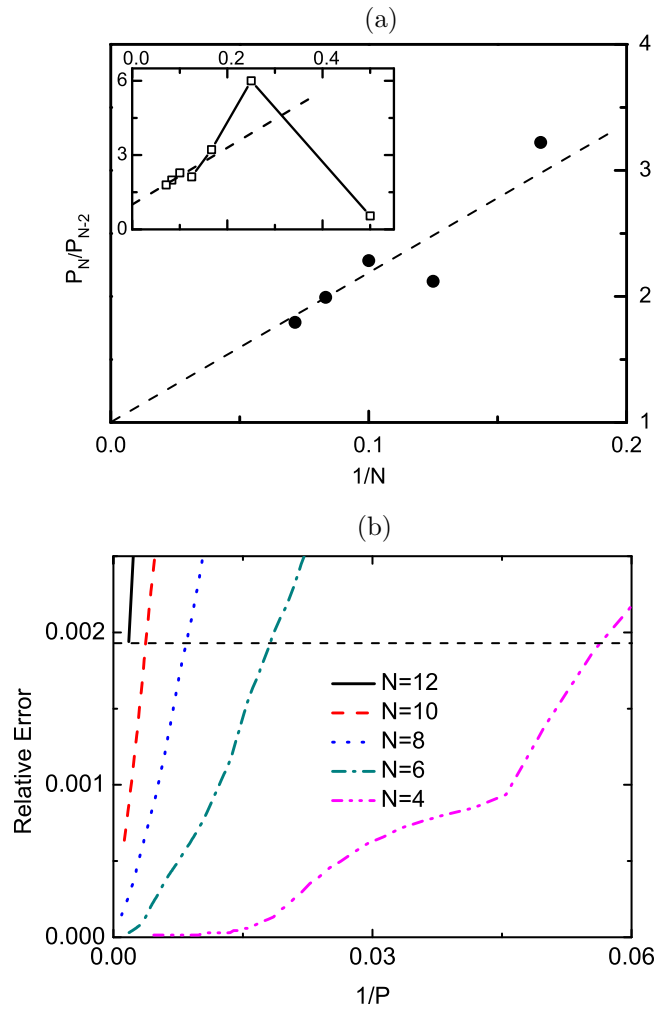

FIG. 12. (a) Ratio of the MPS rank P_N to P_{N-2}, with respect to $\frac{1}{N}$. At both P_N and P_{N-2} the same accuracy is obtained. The tendency of $\frac{P_N}{P_{N-2}} \to 1$ for $\frac{1}{N} \to 0$ implies the saturating MPS rank with increasing N. The inset shows a larger scale starting from $\frac{P_2}{P_1}$. (b) The horizontal dashed line intercepts the curves of "relative error versus $1/P$," giving P_N's used in (a), given certain relative error, say 1.9×10^{-3}. The comparison between $N = 12$ and 14 is made for the relative error of 5.3×10^{-3}, where $P = 195$ for $N = 12$ and $P = 350$ for $N = 14$, respectively.

B. Signature of dimensional transition

We now show that the ladder is still gapped for $N = 8$ and that it is ordered hence gapless for $N \geqslant 10$. We study C_r versus r, where C_r is spin-spin correlation at separation r in LD. Hereafter, we discuss the absolute value of the correlations, despite the fact that they have alternating signs due to the antiferromagnetism.

Figure 14 is shown in the semilogarithmic scale for $N = 2$, 4, and 6. The straight tilted lines indicate exponential decays with respect to the spin-spin separation. Comparison of the spin-spin separation needed for the same value of spin-spin correlation gives the ratio $1 : 4 : 9$ of correlation lengths for these three lattices. It is worth noting the behavior of $N = 6$. It looks straight when $P \leqslant 250$ but then jumps down to the bottom when $P = 270$, and finally converges to

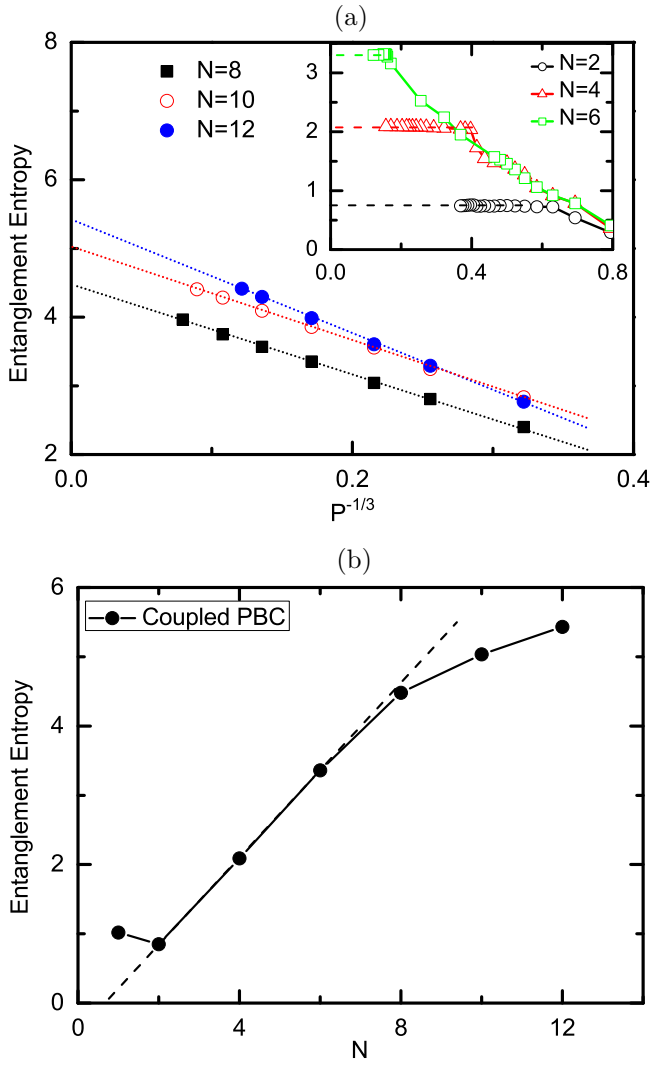

FIG. 13. Entanglement entropy of an effective site for coupled ladders with PBC in the rung. (a) Entanglement entropy versus $P^{-1/3}$. The steady tendency to $P^{-1/3} = 0$ gives extrapolation for $N = 8,\ 10,$ and 12 shown as rectangles, circles, and triangles, respectively. Those of $N = 2,\ 4,$ and 6 from bottom to top in the inset exhibit sudden convergence. (b) Entanglement entropy versus N.

the fixed line. This is a clear indication of the competition between order and disorder.

For $N \geqslant 8$, we did not obtain the converged plot of C_r versus r due to the larger entanglement entropy. For those systems, we study a quantity $\tau_r \equiv \ln(\ln C_r - \ln C_{r+1})$. It is the varying rate of $\ln C_r$. If this rate is a negative constant, the correlation decays exponentially with r. If the rate decreases with r, the correlation is a constant at infinite separation, indicating that the lattice is ordered. Figures 15(b) and 16(c) both show that this quantity is linear with r at various MPS rank P's, as explained in Sec. II H. But, their asymptotic ($P \to \infty$) behaviors are different. For $N = 8$, τ_r asymptotically becomes a negative constant for large r's shown as the dashed curve in Fig. 15(b). This negative constant is obtained when the lines of τ_r versus $P^{-3/4}$ for various large r's converge to the same value when $p \to \infty$ in Fig. 15(a). Starting from $C_1 = \bar{\epsilon}_0/6$ and then tracing along the asymptotic curve in Fig. 15(b), we

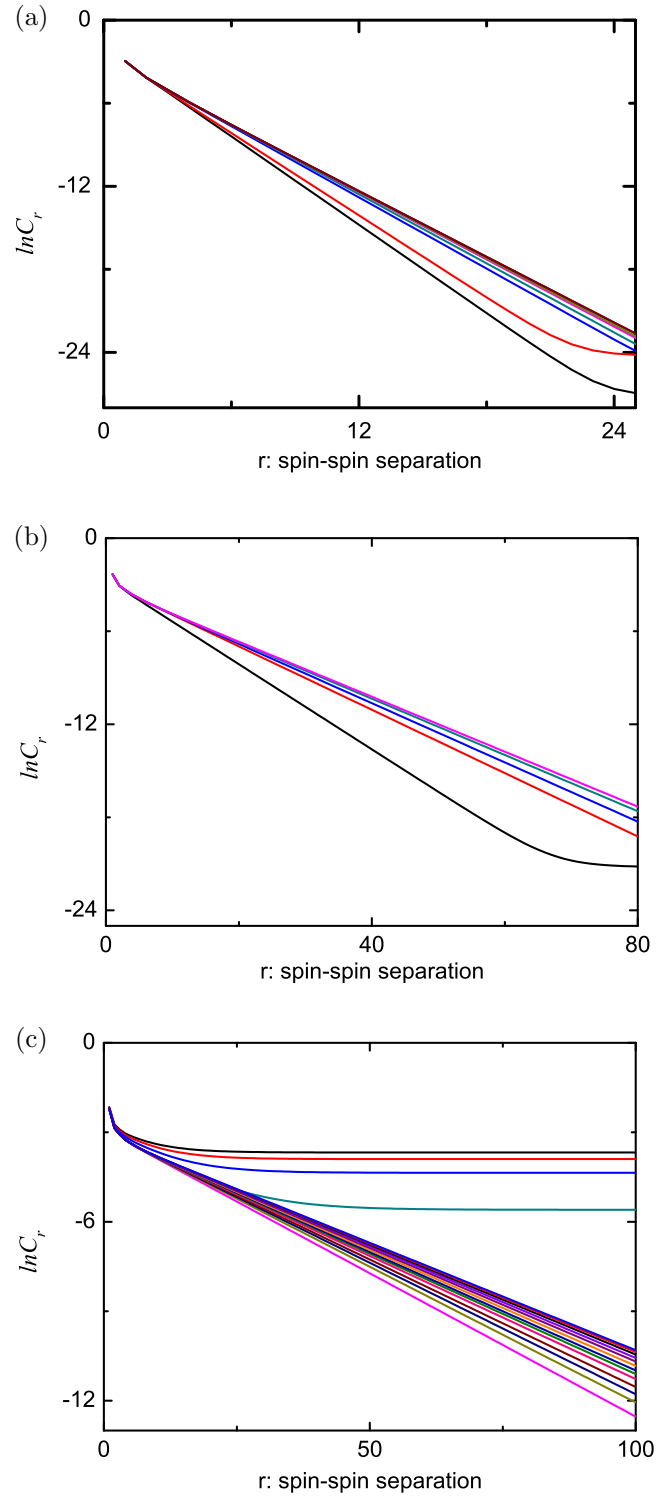

FIG. 14. $\ln C_r$ versus r. The linear tilted lines in logarithmic scale suggest the exponential decay of correlations with respect to separations. They approach the fixed one from bottom when $P = 4$ to top when $P = 28$ (every augment of 4 for P) for $N = 2$ in (a); from bottom when $P = 40$ to top when $P = 200$ (every 40) for $N = 4$ in (b). However, the beginning lines are flat at top in (c) for $N = 6$, starting from top when $P = 190$ to the last flat one in the middle zone when $P = 250$ (every 20). It suddenly jumps down to the tilted line at the bottom when $P = 270$ and approaches the fixed tilted line when $P = 560$ (every 20).

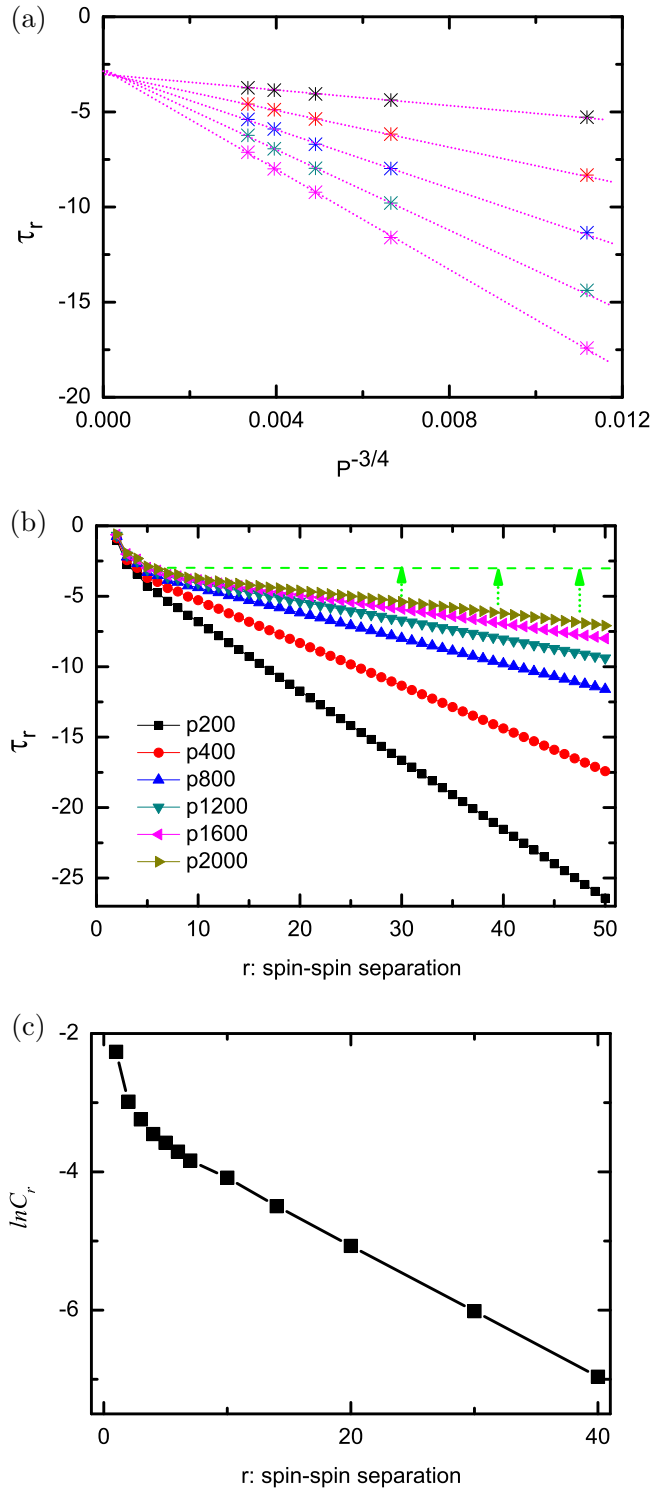

FIG. 15. C_r and $\tau_r \equiv \ln(\ln C_r - \ln C_{r+1})$ for $N = 8$. (a) τ_r versus $P^{-3/4}$ at separations $r = 10, 20, 30, 40$, and 50 from top to bottom. (b) τ_r versus r at various P's. They asymptotically approach the dashed curve obtained by the extrapolation in (a). Trace along the asymptotic curve in (c), starting from $\ln C_1 = \ln\frac{\epsilon_0}{6}$, yields the asymptotic curve of $\ln C_r$ versus r.

obtain the dependence of $\ln C_r$ on r in Fig. 15(c). It is seen that C_r for $N = 8$ decays exponentially with r. Nevertheless, For $N = 10$, Fig. 16(a) shows that the lines of τ_r versus $P^{-3/4}$ do

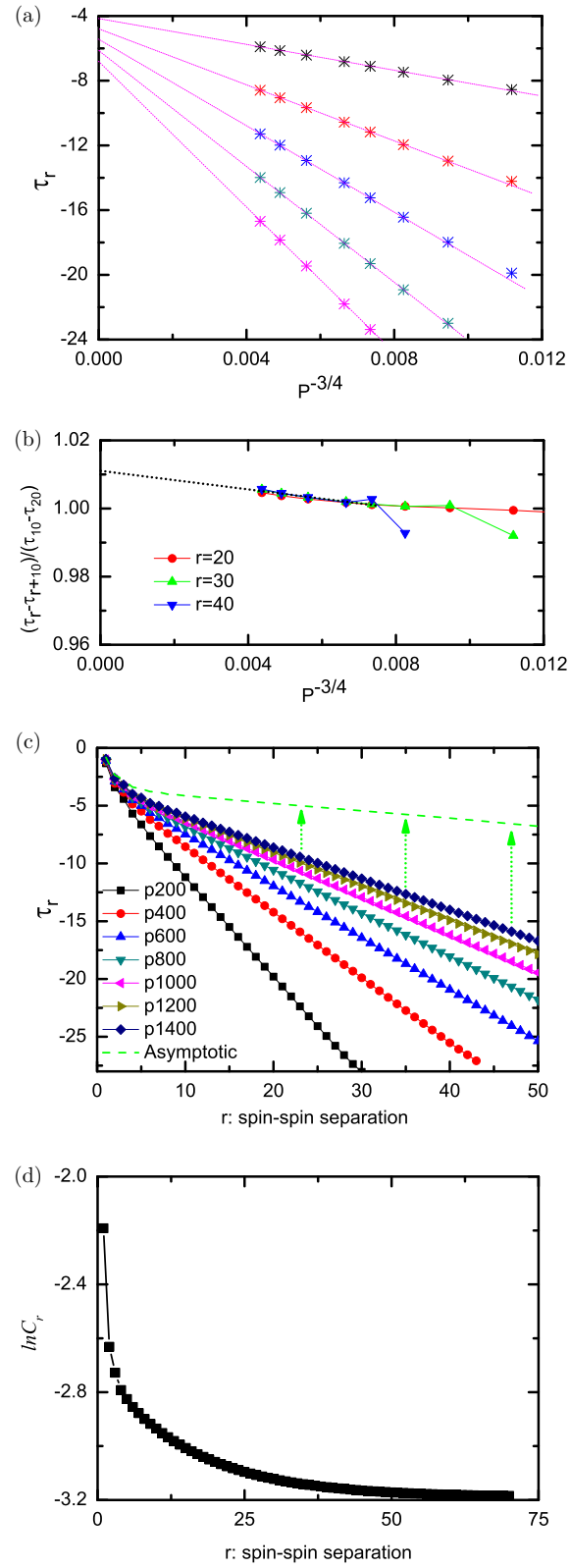

FIG. 16. C_r and $\tau_r \equiv \ln(\ln C_r - \ln C_{r+1})$ for $N = 10$. (a) τ_r versus $P^{-3/4}$ at $r = 10, 20, 30, 40$, and 50 from top to bottom. (b) $(\tau_r - \tau_{r+10})/(\tau_{10} - \tau_{20})$ versus $P^{-3/4}$ at $r = 20, 30$, and 40. (c) τ_r versus r at various P's. They asymptotically approach the dashed curve obtained by the extrapolation in (a). (d) Trace along the asymptotic curve in (c) yields the asymptotic curve of $\ln C_r$ versus r.

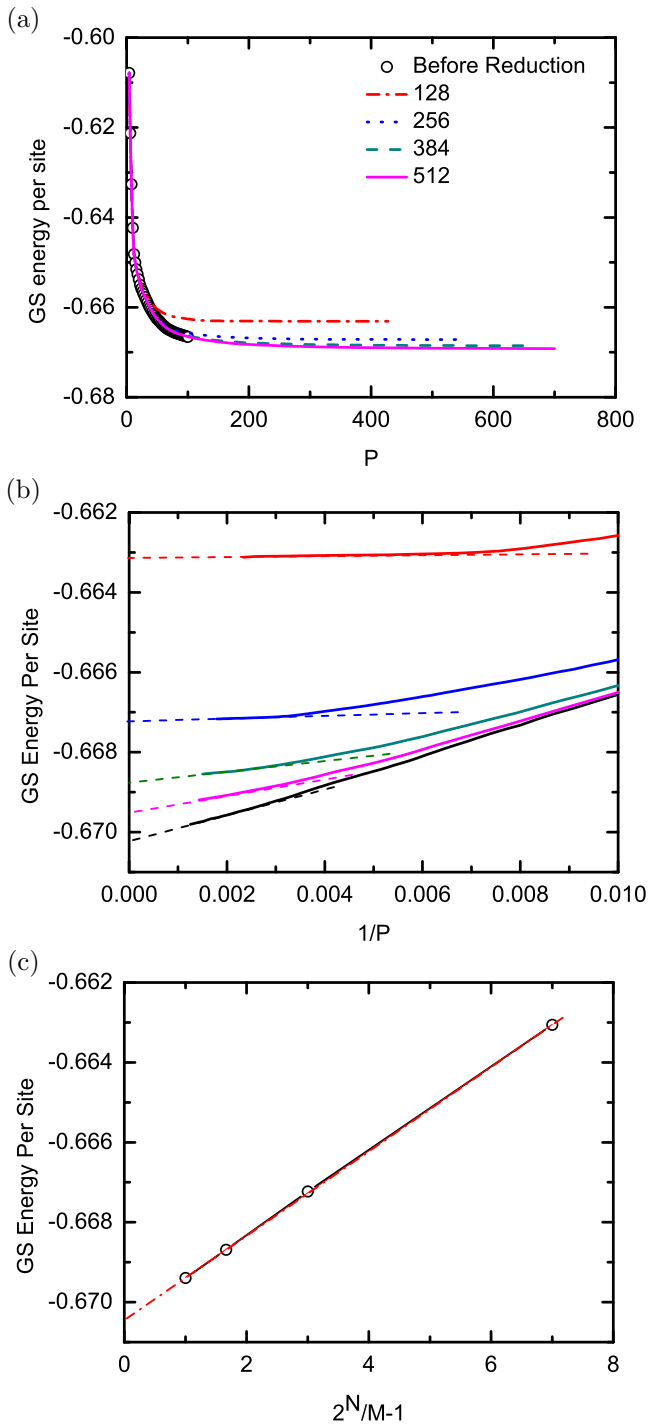

FIG. 17. Effect of space reduction in MPS for $N = 10$. (a) GS energy per site versus MPS rank P. Open circles denote the solution before reduction. Result at $P_1 = 100$ is used to reduce the space rank to 128, 256, 384, and 512, yielding new solutions shown as dotted-dashed, dotted, dashed, and solid curves. (b) GS energy versus $1/P$. Tangents of convergence yield the extrapolated energies for various space ranks, 128, 256, 384, 512, and 1024 (unreduced) from top to bottom. (c) Extrapolation of the energy in unreduced spaces using those obtained in reduced spaces.

not converge to the same value when $p \to \infty$. Figure 16(b) further shows that $\tau_r - \tau_{r+10}$ are equal for $r = 10$, 20, 30, and 40, implying that the lines in Fig. 16(a) are equally

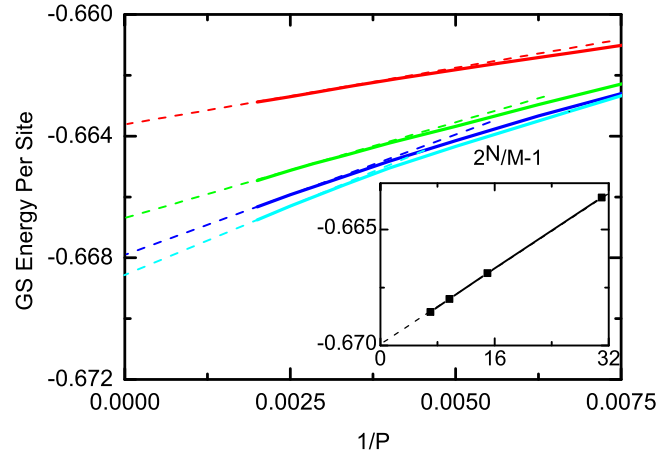

FIG. 18. Use of space reduction in MPS for $N = 14$. Tangents of the convergence of GS energy per site versus $1/P$ yield extrapolated energies for various space ranks, 512, 1024, 1536, and 2048 from top to bottom. The inset extrapolates GS energy per site in the unreduced space using those extrapolations obtained in reduced spaces.

spaced. Thus, the dashed asymptotic curve in Fig. 16(c) has a constant negative slope for large r's. Tracing along the asymptotic curve, we obtain the dependence of $\ln C_r$ on r in Fig. 16(d). $\ln C_r$ hence C_r become a nonzero constant at infinite spin-spin separation. The ladder of $N \geqslant 10$ is ordered. Since no external pinning magnetic field [74] is applied, it implies that the spin-rotational symmetry is spontaneously broken.

Our finding that the lattice of $N \leqslant 6$ is not ordered is fully consistent with the previous report [5] that gaps exist for lattices of $300 \times N$, $N \leqslant 6$. The gap leads to the fast exponential-like decay for spin-spin correlations reported for those lattices. Nevertheless, we show with strong numerical evidence that the spin-rotational symmetry spontaneously breaks for a spin-$\frac{1}{2}$ lattice of $N \geqslant 10$. Since a spontaneously ordered GS is regarded as a 2D characteristic by the existing theories, such as SWT, NLSM, and Mermin-Wager theory [11,12], the spontaneous symmetry breaking defines a quantum dimensional transition from 1D including quasi-1D to 2D at a finite ladder width N.

C. Effects of space reduction in matrix product state

The effect of space reduction in MPS is shown with the example of $N = 10$ in Fig. 17. In Fig. 17(a), simulated data in the original space of rank of 2^{10} are shown with open circles. At $P_1 = 100$, the solution is used to reduce the space rank to 128, 256, 384, and 512 to yield solutions in dotted-dashed, dotted, dashed, and solid curves, respectively. Except for the reduced rank 128, simulations for other reductions reproduce the solution before reduction when $P \leqslant P_1$. The closing gaps between flattening curves are confirmed in Fig. 17(b), where the energies versus $1/P$ are plotted for space ranks 128, 256, 384, and 512 from top to bottom. The simulation in original space is also carried on after P_1, shown as the bottom curve in the same plot. All curves show convergence. The extrapolation by tangents of those converging curves yields energies

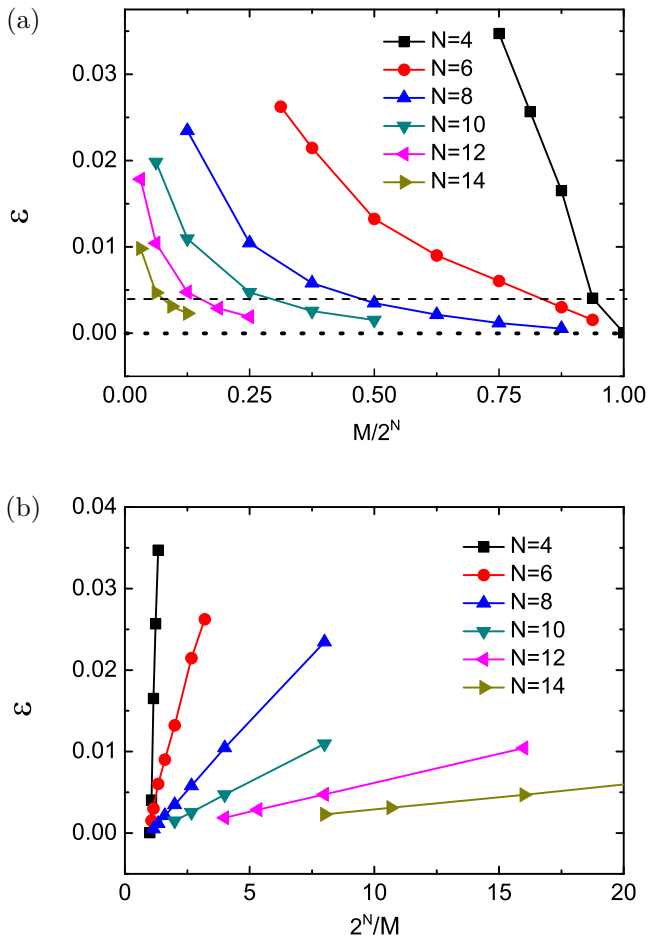

FIG. 19. Relative error versus (a) $M/2^N$ (reduction ratio) and (b) $2^N/M$ (inverse ratio). In (a), the dotted line gives a reference of zero error, while the dashed line intercepts each curve to give the reduction ratio at a certain accuracy. (b) Energies obtained in reduced spaces for lattices of larger N approach more linearly to those in unreduced space. Figures 17(c) and 18 show such examples for $N = 10$ and 14, respectively.

in spaces of both various reduced sizes and the original size. Those in the reduced spaces are used to extrapolate the energy in the unreduced space, as shown in Fig. 17(c). There, the linear fit yields -0.6704, agreeing well with $-0.670\,22$ by extrapolation using the data obtained before space reduction in Fig. 17(b). Note that this scheme, which extrapolates the result in original spaces with the data obtained in reduced spaces, is much more computationally efficient so as to allow simulation at larger-P values.

We run simulations for $N = 14$ in various reduced spaces of ranks 512, 1024, 1536, and 2048 up to $P = 500$, shown from top to bottom in Fig. 18. The lowest energy without extrapolation is $-0.666\,76$ at $P = 500$ in the reduced space of size 2048, lower than the value $-0.666\,36$ in Table II obtained at $P = 350$ that is the largest P value to be handled in the unreduced spaces. Meanwhile, the inset extrapolates to $-0.669\,98$ with the difference of 5×10^{-5} from $-0.669\,93$ which was obtained by the interpolation in Fig. 11(c).

Figure 19(a) shows the result of ϵ versus $M/2^N$ for various M's and N's, where 2^N is the original space rank; ϵ is the relative error between the energies obtained before and after reduction. It is seen that, for $N = 12$, only $1/8$ of the original space size 2^{12} is needed to achieve a relative error of 4.1×10^{-3}. In comparison, the same accuracy for $N = 4$ is obtained with 15 out of 2^4 basis vectors. For $N = 2$, no reduction will achieve good accuracy. Figure 19(b) shows the dependence of relative error on $2^N/M$. Larger lattices ($N \geqslant 8$) show a linear dependence, which is a reconfirmation for the reliability of extrapolating results using simulation in reduced spaces. Figures 17(b) and 17(c) illustrate such an example for a lattice of $N = 10$. Figure 18 shows another example for $N = 14$.

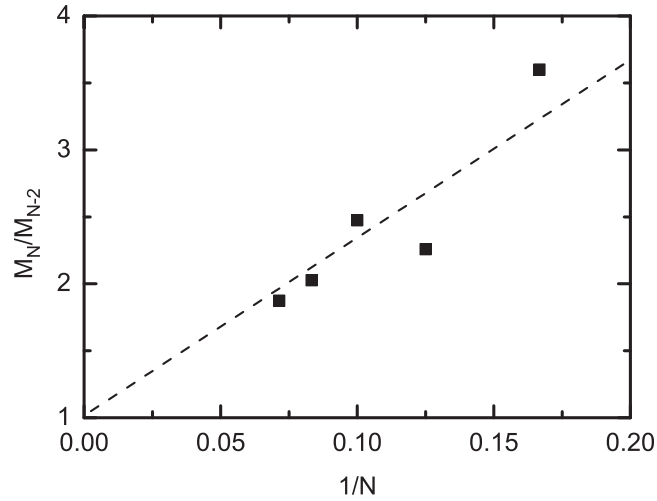

FIG. 20. Ratio of basis vector numbers kept for N and $N-2$, respectively, versus $1/N$. The linear fit overlaps with the guiding dashed line to 1 when $N \to \infty$.

We plot in Fig. 20 M_N/M_{N-2} (ratio of numbers of basis vectors kept to achieve the same accuracy for N and $N-2$, respectively) versus $1/N$. It shows that this ratio tends to approach 1 when $N \to \infty$. As discussed in Sec. II D, a saturating number of significant diagonal density matrix elements of an effective site is responsible for the saturating entanglement entropy and consequently for the saturating MPS rank P, when N increases. Figures 12(b) and 20 are indeed consistent.

V. CONCLUSION

In conclusion, the way we treated the $\infty \times N$ quantum lattice as 1D effective lattice, converting N lattices in the rung into an effective site, enables us to handle the unprecedented lattice sizes with N up to 14. We show that both the number of significant diagonal density matrix elements and the entanglement entropy of an effective site saturate with increasing N. The former is responsible for the latter. It bypasses the area law of entanglement entropy for the 2D quantum lattice. Our results for such a lattice with OBC along the rungs are progressively more accurate for larger N's than DMRG.

For the target model with PBC both along the rungs and LD, the prediction of NLSM that the lattice will have a gap which exponentially decays with N until $N \to \infty$ is shown to only fully apply to $N \leqslant 6$ and partially apply to $N = 8$ whose gap does not decay exponentially. In contrast, our data revealed the signature of a quantum dimensional transition

from 1D (including quasi-1D) to 2D that takes place at a critical width $N = 10$, with emerging [4] order parameters.

VI. OUTLOOK

The saturating entanglement guarantees that the MPS rank, which otherwise exponentially increases with N, saturates as well, relieving the major computational burden related to the MPS size. It is instructive to exhaust other factors which will cause an exponential growth of computational burden with respect to N in this method. The first such factor is the linking complexity in MPO that in this work is reduced to a linear relationship with N by the entanglement perturbation of MPO. The second and also the last such factor is the exponentially increasing number of local quantum states on the effective site. It is 2^N for spin-$\frac{1}{2}$. The limited number of significant diagonal density matrix elements of an effective site enables an efficient reduction of the space in MPS, hence eliminating the last exponential factor in this method. It is possible that a 2D $\infty \times \infty$ quantum lattice physically behaves like a 1D lattice which has limited significant local states on a slice and is linked with limited entanglement between neighboring slices, when looked from any direction of its two dimensions. The method used in this work is a promising numerical tool when studying strong correlations in 2D in this way.

In addition, the emerging local magnetization in those $\infty \times N$ lattices with $N \geqslant 10$ shows different finite-size effect from that of an $N \times N$ or $\alpha N \times N$ [74] (α is a small integer) lattice. Since no pinning magnetic field B is needed, extrapolating to the thermodynamic limit will be simpler. Staggered magnetization, one of the most fundamental physical quantities for quantum spins, warrants more investigation along this line.

Note that the space reduction in MPS shown in this study can be readily extended to any form of MPS or TNS based methods such as PEPS, whenever they are built on a blocked quantum system.

ACKNOWLEDGMENTS

This work was supported by NRF (National Honor Scientist Program Grant No. 2010-0020414) and KISTI (Grants No. KSC-2018-CHA-0077, No. KSC-2018-CHA-0057, No. KSC-2017-C3-0081, No. KSC-2016-C3-0074, No. KSC-2015-C3-002, No. KSC-2014-C3-019). We thank D. C. Yang for valuable discussion.

APPENDIX: CORRELATIONS WITH MPS QUANTITIES

Bosonization [32,33] predicts a power-law decay of spin-spin correlations $C(r) \propto r^{-1}$ for an antiferromagnetic spin-$\frac{1}{2}$ chain, r being the spin-spin separation. So, the spin chain has QLRO. In Sec. II H we discussed in the framework of MPS that the eigenvalue structure of the building unit B [defined in the second equation of (9)] for $\langle g|g\rangle$ is responsible for spin-spin correlations, where $|g\rangle$ is the GS.

Figure 21(a) shows F_j's defined in Eq. (73) for the first 100 largest eigenvalues of B. Only a few are significant in magnitude. In the inset, the ratio ϱ_j/ϱ_1 versus j shows that a few largest eigenvalues are almost degenerate with ϱ_1. We then plot C_r versus r for spin chain in Fig. 21(b). The

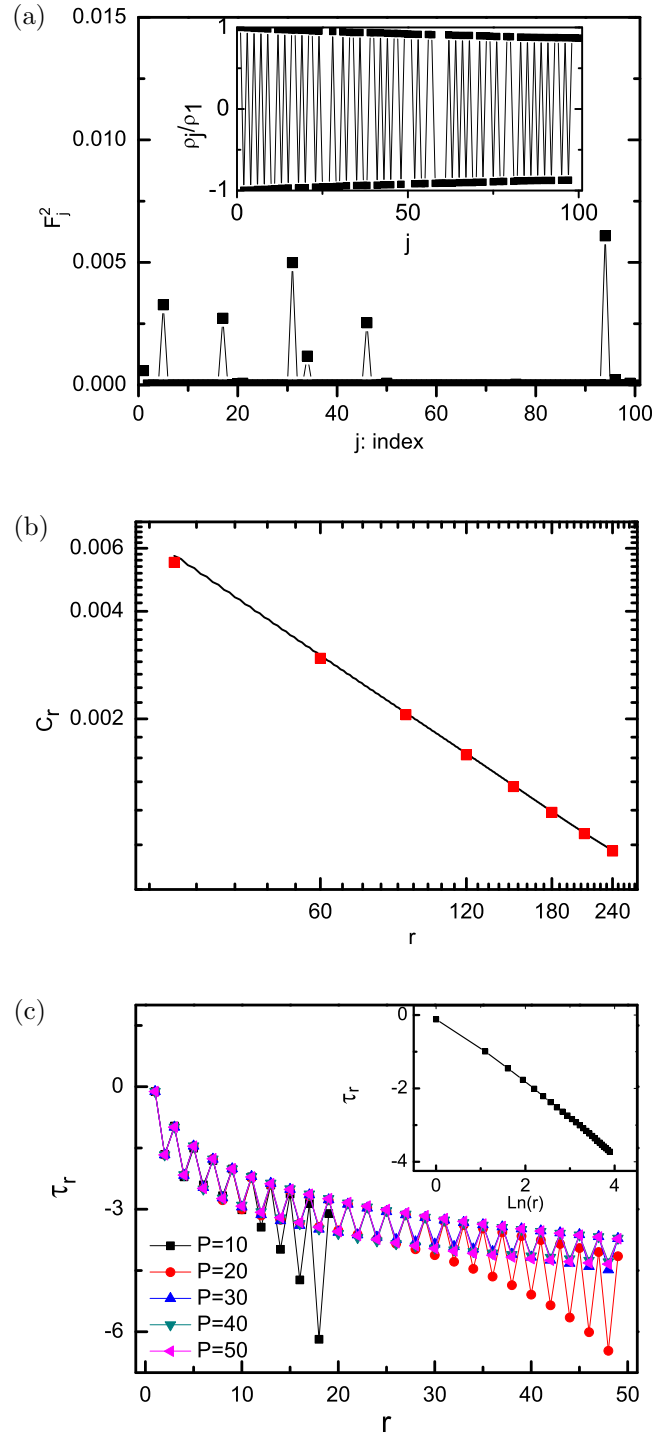

FIG. 21. QLRO correlations of a spin chain. (a) The largest few eigenvalues, which are shown in inset to be nearly degenerate with ϱ_1, have less significant F_j's. They make small contributions to C_r that slowly decay with r. The eigenvalues which have significant F_j's are definitely smaller than ϱ_1. They make contributions that are large at smaller r's but decay rapidly with r. (b) The solid line in the log-log view of C_r versus r collects contributions to C_r from all eigenvalues. Rectangles collect contributions only from those mentioned in (a). (c) $\tau_r \equiv \ln(\ln C_r - \ln C_{r+1})$ versus r. The inset takes the odd branch as an example to show τ_r is linear with $\ln(r)$, in sharp contrast to the linear dependence of τ_r on r for both disorder and order.

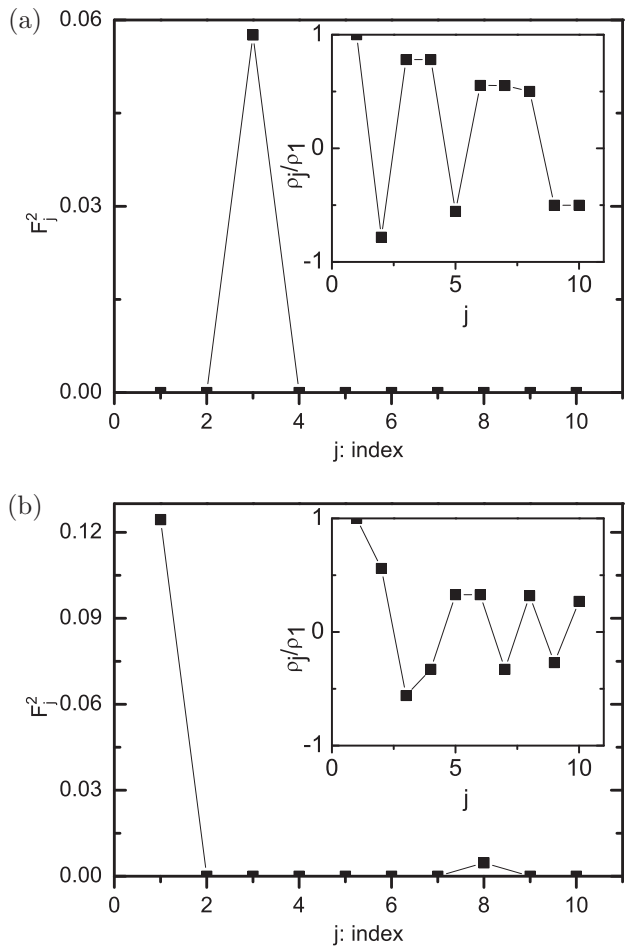

FIG. 22. Eigenvalue structure of B for (a) the disordered spin ladder of $N = 4$ and (b) the ordered ladder of $N = 10$.

linear solid line in log-log view is obtained according to Eq. (67), showing a power-law decay. This result contains contributions from all eigenvalues of B. Nevertheless, the rectangles represent data that only collects the contributions from a few largest eigenvalues, that are nearly degenerate with ϱ_1 but have less significant F's, and from those that are definitely smaller than ϱ_1 but have more significant F's shown as spikes in Fig. 21(a). The slowly varying constant-like correlation contribution by the former adds up with the fast exponentially decaying correlation contribution by the latter, reproducing the power-law decay in a large range of r. Meanwhile, Fig. 21(c) plots τ_r defined in Eq. (72) versus r. The odd and even series both converge with the MPS rank P to nonlinear curves. The inset shows that, for instance, the odd series of τ versus $\ln(r)$ is linear. It is in sharp contrast to the linear dependence of τ on r of either disorder [Fig. 15(b)] or order [Fig. 16(c)].

Figure 22 shows the eigenvalue structure of B for disorder in Fig. 22(a) and order in Fig. 22(b). For the disordered spin ladder of $N = 4$ in Fig. 22(a), only the third largest eigenvalue of B has nonvanishing F_3 shown as the spike. Inset shows that ϱ_3/ϱ_1 is significantly smaller than 1. It leads to the exponential decay of C_r to zero for large r, making τ_r a constant. If F_1 is not converged with the MPS rank P yet and hence does not vanish, it will be a small value compared to F_3. τ_r linearly decreases with r. The decreasing rate asymptotically becomes zero when $P \to \infty$. See Fig. 15 for such an example of $N = 8$. For the ordered spin ladder of $N = 10$ in Fig. 22(b), only the first and eighth largest eigenvalues of B have nonvanishing F_1 and F_8 shown as the spikes. ϱ_8/ϱ_1 is significantly smaller than 1 in inset. It belongs to Case 1 described in Sec. II H. $\ln C_r$ exponentially decays to a nonzero constant when r is large, as Fig. 16 shows. Thus, the lattice has a nonvanishing correlation even at infinite separation and is therefore ordered.

[1] Y. Jompol, C. J. B. Ford, J. P. Griffiths, I. Farrer, G. A. C. Jones, D. Anderson, D. A. Ritchie, T. W. Silk, and A. J. Schofield, Science **325**, 597 (2009).
[2] I. Gross, W. Akhtar, V. Garcia, L. J. Martínez, S. Chouaieb, K. Garcia, C. Carrétéro, A. Barthélémy, P. Appel, P. Maletinsky *et al.*, Nature (London) **549**, 252 (2017).
[3] H. Bethe, Z. Phys. **71**, 205 (1931).
[4] P. W. Anderson, Science **177**, 393 (1972).
[5] M. Greven, R. J. Birgeneau, and U. J. Wiese, Phys. Rev. Lett. **77**, 1865 (1996); the studied spin ladders have length up to 300 that mimics the infinite length needed to conclude the disorder. In fact, the order parameter is not really zero in the studied finite systems.
[6] E. Manousakis, Rev. Mod. Phys. **63**, 1 (1991).
[7] L. M. Hoang and J. M. Baranowski, Phys. Status Solidi B **84**, 361 (1977).
[8] Y. F. Kung, C. Bazin, K. Wohlfeld, Y. Wang, C.-C. Chen, C. J. Jia, S. Johnston, B. Moritz, F. Mila, and T. P. Devereaux, Phys. Rev. B **96**, 195106 (2017).
[9] M. Raczkowski and F. F. Assaad, Phys. Rev. B **88**, 085120 (2013).
[10] S. M. Disseler, Y. Chen, S. Yeo, G. Gasparovic, P. M. B. Piccoli, A. J. Schultz, Y. Qiu, Q. Huang, S.-W. Cheong, and W. Ratcliff, Sci. Rep. **5**, 17771 (2015).
[11] N. D. Mermin and H. Wagner, Phys. Rev. Lett. **17**, 1133 (1966).
[12] S. Coleman, Commun. Math. Phys. **31**, 259 (1973).
[13] M. Vojta, N.-H. Tong, and R. Bulla, Phys. Rev. Lett. **94**, 070604 (2005).
[14] G.-S. Tian, Phys. Rev. B **56**, 5355 (1997).
[15] A. K. Kolezhuk, H.-J. Mikeska, and S. Yamamoto, Phys. Rev. B **55**, R3336 (1997).
[16] F. J. Dyson, E. H. Lieb, and B. Simon, J. Stat. Phys. **18**, 4 (1978).
[17] B. S. Shastry, J. Phys. A: Math. Gen. **25**, L249 (1992).
[18] T. Kennedy, E. H. Lieb, and B. S. Shastry, J. Stat. Phys. **53**, 1019 (1988).
[19] Y. Ozeki, H. Nishimori, and Y. Tomita, J. Phys. Soc. Jpn. **58**, 82 (1989).

[20] J. R. Parreira, O. Bolina, and J. F. Perez, J. Stat. Phys. **86**, 5 (1997).
[21] E. Neves and J. Perez, Phys. Lett. A **114**, 331 (1986).
[22] J. R. Parreira, O. Bolina, and J. F. Perez, J. Phys. A: Math. Gen. **30**, 1095 (1997).
[23] E. S. Sørensen and I. Affleck, Phys. Rev. Lett. **71**, 1633 (1993).
[24] S. Yamamoto, Phys. Rev. Lett. **75**, 3348 (1995).
[25] S. Chakravarty, Phys. Rev. Lett. **77**, 4446 (1996).
[26] G. Sierra, J. Phys. A **29**, 3299 (1996).
[27] S. R. White, R. M. Noack, and D. J. Scalapino, Phys. Rev. Lett. **73**, 886 (1994).
[28] E. Dagotto and T. M. Rice, Science **271**, 618 (1996).
[29] E. Stoudenmire and S. R. White, Annu. Rev. Condens. Matter Phys. **3**, 111 (2012).
[30] F. B. Ramos and J. C. Xavier, Phys. Rev. B **89**, 094424 (2014).
[31] N. Landsman, Stud. Hist. Philos. Sci. B Stud. Hist. Philos. Modern Phys. **44**, 379 (2013).
[32] A. Luther and I. Peschel, Phys. Rev. B **9**, 2911 (1974).
[33] A. Luther and I. Peschel, Phys. Rev. B **12**, 3908 (1975).
[34] I. Affleck, D. Gepner, H. J. Schulz, and T. Ziman, J. Phys. A: Math. Gen. **23**, 4725 (1990).
[35] I. Affleck, J. Phys. A: Math. Gen. **31**, 4573 (1998).
[36] L. Wang and S. G. Chung, J. Phys. Soc. Jpn. **81**, 114712 (2012).
[37] D. G. Shelton, A. A. Nersesyan, and A. M. Tsvelik, Phys. Rev. B **53**, 8521 (1996).
[38] A. L. Chernyshev and M. E. Zhitomirsky, Phys. Rev. B **79**, 144416 (2009).
[39] L. Wang and S. G. Chung, arXiv:1110.0377v2.
[40] D. M. Ceperley and B. J. Alder, Phys. Rev. Lett. **45**, 566 (1980).
[41] S. R. White, Phys. Rev. Lett. **69**, 2863 (1992).
[42] S. R. White, Phys. Rev. B **48**, 10345 (1993).
[43] S. Furukawa, M. Sato, and A. Furusaki, Phys. Rev. B **81**, 094430 (2010).
[44] L. Wang and S. G. Chung, Int. J. Mod. Phys. B **29**, 1550042 (2015).
[45] T. Kariyado and Y. Hatsugai, Phys. Rev. B **91**, 214410 (2015).
[46] T. Nishino, K. Okunishi, Y. Hieida, N. Maeshima, and Y. Akutsu, Nucl. Phys. B **575**, 504 (2000).
[47] Y. Nishio, N. Maeshima, A. Gendiar, and T. Nishino, arXiv:cond-mat/0401115v1.
[48] J. Jordan, R. Orús, G. Vidal, F. Verstraete, and J. I. Cirac, Phys. Rev. Lett. **101**, 250602 (2008).
[49] Q.-Q. Shi, H.-L. Wang, S.-H. Li, S. Y. Cho, M. T. Batchelor, and H.-Q. Zhou, Phys. Rev. A **93**, 062341 (2016).
[50] G. Ehlers, S. R. White, and R. M. Noack, Phys. Rev. B **95**, 125125 (2017).
[51] S.-H. Li, Q.-Q. Shi, Y.-H. Su, J.-H. Liu, Y.-W. Dai, and H.-Q. Zhou, Phys. Rev. B **86**, 064401 (2012).
[52] M. Fannes, B. Nachtergaele, and R. F. Werner, Commun. Math. Phys. **144**, 443 (1992).
[53] S. Östlund and S. Rommer, Phys. Rev. Lett. **75**, 3537 (1995).
[54] F. Verstraete, D. Porras, and J. I. Cirac, Phys. Rev. Lett. **93**, 227205 (2004).
[55] S. Chung, Phys. Lett. A **359**, 707 (2006).
[56] S. Chung, Phys. Lett. A **361**, 396 (2007).
[57] S. G. Chung and L. Wang, Phys. Lett. A **373**, 2277 (2009).
[58] D. Perez-Garcia, F. Verstraete, M. M. Wolf, and J. I. Cirac, Quantum Inf. Comput. **7**, 401 (2007).
[59] G. M. Crosswhite, A. C. Doherty, and G. Vidal, Phys. Rev. B **78**, 035116 (2008).
[60] I. P. McCulloch, arXiv:0804.2509v1.
[61] J. Eisert, M. Cramer, and M. B. Plenio, Rev. Mod. Phys. **82**, 277 (2010).
[62] U. Schollwöck, Rev. Mod. Phys. **77**, 259 (2005).
[63] F. Verstraete, J. J. García-Ripoll, and J. I. Cirac, Phys. Rev. Lett. **93**, 207204 (2004).
[64] B. Pirvu, V. Murg, J. I. Cirac, and F. Verstraete, New J. Phys. **12**, 025012 (2010).
[65] G. L. G. Sleijpen, A. G. L. Booten, D. R. Fokkema, and H. A. van der Vorst, BIT Numer. Math. **36**, 595 (1996).
[66] G. Knizia and G. K.-L. Chan, Phys. Rev. Lett. **109**, 186404 (2012).
[67] W. Metzner and D. Vollhardt, Phys. Rev. Lett. **62**, 324 (1989).
[68] T. A. Kaplan, P. Horsch, and W. von der Linden, J. Phys. Soc. Jpn. **58**, 3894 (1989).
[69] B. Frischmuth, B. Ammon, and M. Troyer, Phys. Rev. B **54**, R3714 (1996).
[70] S. Irani, J. Math. Phys. **51**, 022101 (2010).
[71] D. Gottesman and M. B. Hastings, New J. Phys. **12**, 025002 (2010).
[72] R. R. P. Singh and D. A. Huse, Phys. Rev. B **40**, 7247 (1989).
[73] U. J. Wiese and H. P. Ying, Z. Phys. B **93**, 147 (1994).
[74] S. R. White and A. L. Chernyshev, Phys. Rev. Lett. **99**, 127004 (2007).